Comparison of different global information sources used in surface radiative flux calculation: Radiative properties of the surface

Yuanchong Zhang,[1] William B. Rossow,[2] and Paul W. Stackhouse Jr.[3]

[1]   Direct estimates of surface radiative fluxes that resolve regional and weather-scale variability over the whole globe with reasonable accuracy have only become possible with the advent of extensive global, mostly satellite, data sets within the past couple of decades. The accuracy of these fluxes, estimated to be about $10-15$ W/m^2, is largely limited by the accuracy of the input data sets. The leading uncertainties in the surface fluxes are no longer predominantly induced by clouds but are now as much associated with uncertainties in the surface and near-surface atmospheric properties. This study presents a fuller, more quantitative evaluation of the uncertainties for the surface albedo and emissivity and surface skin temperatures by comparing the main available global data sets from the Moderate-Resolution Imaging Spectroradiometer product, the NASA Global Energy and Water Cycle Experiment Surface Radiation Budget project, the European Centre for Medium-Range Weather Forecasts, the National Aeronautics and Space Administration, the National Centers for Environmental Prediction, the International Satellite Cloud Climatology Project (ISCCP), the Laboratoire de Météorologie Dynamique, NOAA/NASA Pathfinder Advanced Very High Resolution Radiometer project, and the NOAA Optimum Interpolation Sea Surface Temperature Analysis and the Tropical Rainfall Measuring Mission (TRMM) Microwave Image project. The data sets are, in practice, treated as an ensemble of realizations of the actual climate such that their differences represent an estimate of the uncertainty in their measurements because we do not possess global "truth" data sets for these quantities. The results are globally representative and may be taken as a generalization of our previous ISCCP-based uncertainty estimates for the input data sets. Surface properties have the primary role in determining the surface upward shortwave (SW) and longwave (LW) flux.From this study the following conclusions are obtained. Although land surface albedos in the near-infrared remain poorly constrained (highly uncertain), they do not cause too much error in total surface SW fluxes; the more subtle regional and seasonal variations associated with vegetation and snow are still in doubt. The uncertainty of the broadband black-sky SW albedo for land surface from this study is about 7%, which can easily induce $5-10$ W/m^2 uncertainty in (upwelling) surface SW flux estimates. Even though available surface (broadband) LW emissivity data sets differ significantly ($3-5$% uncertainty), this disagreement is confined to wavelengths >20 μm so that there is little practical effect ($1-3$ W/m^2) on the surface upwelling LW fluxes. The surface skin temperature is one of two leading factors that cause problems with surface LW fluxes. Even though the differences among the various data sets are generally only $2-4$ K, this can easily cause $10-15$ W/m^2 uncertainty in calculated surface (upwelling) LW fluxes. Significant improvements could be obtained for surface LW flux calculations by improving the retrievals of (in order of decreasing importance): (1) surface skin temperature, (2) surface air and near-surface-layer temperature, (3) column precipitable water amount, and

[1]Department of Applied Physics and Applied Mathematics (APAM), Columbia University, at NASA Goddard Institute for Space Studies, New York, New York, USA.
[2]NASA Goddard Institute for Space Studies, Columbia University, New York, New York, USA.
[3]NASA Langley Research Center, Hampton, Virginia, USA.

(4) broadband emissivity. In addition, for surface SW fluxes, improvements could be obtained (excluding improved cloud treatment) by improving the retrievals of (1) aerosols (from our sensitivity studies but not discussed in this work) and (2) surface (black-sky) albedo, of which the NIR part of the spectrum has much larger uncertainty.

1. Introduction

[2] Analyses of global satellite products have resulted in the production of several extensive and detailed surface radiative flux data sets [*Rossow and Lacis*, 1990; *Darnell et al.*, 1992; *Whitlock et al.*, 1995; *Rossow and Zhang*, 1995; *Stackhouse et al.*, 2004; *Zhang et al.*, 2004]. However, the usefulness of these flux products for monitoring long-term variations of global radiation budgets and climate changes, as well as in other applications such as biological and oceanic modeling, is dependent on two separate issues: (1) the current uncertainty (or reliability) that can be estimated by evaluation of the calculated radiative fluxes against more direct measurements and (2) how much and by what means may the flux products be improved. To address the first issue, *Zhang et al.* [1995, 2004] have compared their flux products against surface (and the top of atmosphere) flux observations to estimate their uncertainty. Their 2004 estimate is about $10-15$ W/m^2 uncertainty for surface fluxes. For the second issue, they have conducted all the important sensitivity studies by varying the input data sets (and the radiative transfer model parameters) to provide quantitative uncertainty estimates of the impacts of realistically assumed uncertainties of the input data sets. The realistically assumed uncertainties for the input data sets were based on earlier estimates, mainly from the International Satellite Cloud Climatology Project (ISCCP) D1 [*Rossow and Schiffer*, 1991]. Some of their conclusions are summarized here. (1) Although clouds have, for a long time, been highlighted as the major source of uncertainty in both planetary and surface radiation budgets, the advent of extensive cloud data sets has reduced this source of uncertainty. (2) As a result, other uncertainty sources have now become relatively more important and comparable to the uncertainty from cloud data sets. (3) For surface radiative flux estimates in particular, the accuracy is now largely limited by two aspects of Earth observations that have long been assumed to be adequately observed, especially during the satellite era, namely, the near-surface atmospheric radiative properties (temperature and humidity) that are usually obtained from atmospheric profiling instruments and the surface radiative properties (surface skin temperature, solar albedo and infrared emissivity).

[3] *Zhang et al.* [2006] have presented a fuller, more quantitative evaluation of the uncertainties for the near-surface air temperature and humidity by comparing the main available global data sets that are treated as an ensemble of realizations of the actual climate such that their differences represent an estimate of the uncertainty in their values. Here we follow the same methodology to make such comparisons for the surface properties (section 2). In section 3 we briefly summarize the uncertainties of the surface radiation budget induced by the uncertainties of these input data sets and discuss some implications for understanding and modeling the surface-atmosphere interactions.

2. Surface Radiative Properties

[4] The five major global data sets (three from reanalysis and two from satellite retrieval), used in the comparison for near-surface atmospheric properties in our companion paper [*Zhang et al.*, 2006], also supply other parameters such as surface skin temperature and surface albedo, which are to be compared in this work (with some additional data sets). They are (1) the first version of the ECMWF reanalysis for a 15-year period (1979–1993, called ERA15 or ER in our figures/tables) [*Gibson et al.*, 1999], (2) the first version of the NASA Data Assimilation Office (DAO) Goddard Earth Observing System (GEOS) reanalysis for a 15-year period (March 1980 to February 1995, called GEOS-1 or GE in our figures/tables) [*Takacs et al.*, 1994], (3) the second version of the National Centers for Environmental Prediction reanalysis for a 51-year period (1948–1998, called NCEP or NC in our figures/tables) [*Kistler et al.*, 2001], (4) a version of TOVS from the International Satellite Cloud Climatology Project (ISCCP, thereafter ISCCP-TOVS) [*Rossow et al.*, 1996] that is combined with the modified surface skin and air temperature from ISCCP-FD [*Zhang et al.*, 2004], called ISCCP-FD-TOVS, shortened as FDTV (called TV in some figures/tables, and (5) 3I data set from the Laboratoire de Météorologie Dynamique (LMD) group, who has developed a new analysis that produced temperature and humidity profiles data set from TOVS (Path B) (consisting of the High resolution Infrared Radiation Sounder (HIRS), the Microwave Sounding Unit (MSU) and the Stratospheric Sounding Unit (SSU)) based on Improved Initialization Inversion (therefore, 3I) retrieval algorithm [see *Scott et al.*, 1999]. For more details of these five data sets, see *Zhang et al.* [2006]. To simplify the presentation, unless otherwise indicated, we restrict the comparisons to monthly means and, if available, monthly-hourly means for every sixth hour (UTC = 0, 6, 12, and 18 hours), for January, April, July, and October 1992. Except for some long-term variations in the character of these data sets that we note below, this year is taken to be typical of these products.

2.1. Albedo

[5] The surface albedo, as defined by the ratio of the reflected to incident flux density at surface and reported from measurements or calculations, is usually the apparent albedo that is governed by the radiative interactions between atmospheric multiple scattering and absorption and surface reflection and absorption under specific atmospheric conditions (including clouds) and is also solar zenith angle dependent. As a result, it is highly variable in time because of the rapid variation of atmospheric conditions and

the slower variations of surface conditions. For theoretical and practical uses, particularly in radiation modeling that can account for multiple scattering, there has long been used the physical concept of a surface albedo without atmospheric (including clouds) effects. Though, this quantity is sometimes referred to "surface albedo" without clarification by many authors, a number of authors have actually distinguished it from the apparent albedo by using different names, e.g., "black-sky albedo" (BSA, as chosen in this study) [*Jin et al.*, 2003b], "true albedo" [*Henderson-Sellers and Wilson*, 1983], and "inherent albedo" [*Liang et al.*, 1999]. Thus BSA is the intrinsic property of the surface material (but still varies with solar zenith angle), independent of the properties of any overlying layer (atmosphere). Confusion arises when people use the word "albedo" and neglect the difference between the apparent and black-sky albedo. *Henderson-Sellers and Wilson* [1983] actually pointed out: "Atmospheric scatter tends to increase observed clear-sky system albedo compared with true surface albedo." Sometimes, people just simply and approximately take "clear-sky albedo" (which is a special case of the apparent albedo, but still is very sensitive to the aerosol loading and humidity profile in the atmosphere) as BSA. Note BSA is the apparent albedo for the moon's surface or for other no-atmosphere planets. To derive surface BSA from actual measurements on the Earth, the measured (apparent) albedo values must be "corrected" to eliminate all atmospheric multiple scattering and absorbing effects, including shifts of the spectrum of illumination and the contribution from multiply scattered radiation. BSA is widely used because it is BSA that is specified in a radiative transfer model for calculating shortwave (SW) fluxes. In the following text, we use "albedo" alone when it is for general purposes, meaning that it can be any one of the different albedos or when the precise meaning is not known, while we use BSA or clear-sky albedo in a precise way. Similarly, the longwave (LW, terrestrial radiation wavelengths) surface emissivity can be determined with or without atmospheric effects (no-atmosphere or "black-sky emissivity", section 2.2).

2.1.1. Data Sets

[6] Since the advent of satellites, various global, broadband, land surface albedo products have been derived either from satellite measurements alone (e.g., *Staylor and Wilber* [1990], *Li and Garand* [1994], both from the Earth Radiation Budget Experiment (ERBE), and *Jin et al.* [2003b], from the Moderate-Resolution Imaging Spectroradiometer (MODIS)), or from a combination of the surface spectral reflectivity properties for different surface types, compiled from surface, airborne, satellite and laboratory measurements, and classification of each location by vegetation-soil types [e.g., *Csiszar and Gutman*, 1999; *Zhang et al.*, 1995]. The latter approach is used in virtually all weather forecast and climate models. Both methods (or some combination) are used by various authors in their calculations of surface and/or the top of the atmosphere (TOA) SW fluxes [e.g., *Rossow and Lacis*, 1990; *Darnell et al.*, 1992; *Pinker and Laszlo*, 1992; *Whitlock et al.*, 1995; *Zhang et al.*, 1995; *Chen and Roeckner*, 1996; *Gupta et al.*, 2001; *Zhang et al.*, 2004].

[7] ERA15 used an albedo map [*Gibson et al.*, 1999] determined from a background yearly climatology with fixed values of 0.55 for sea ice and 0.07 for open water. For land the albedo varies between 0.07 and 0.80 whenever snow occurs, but the albedo for snow-free vegetation is constant all year long, based on surface vegetation classification. GEOS-1 specifies its surface albedos from *Posey and Clapp* [1964] with some modifications for land and fixed values of 0.07 and 0.80 for open water and sea ice, respectively. For snow cover, albedo is usually greater than 0.4 [*Takacs et al.*, 1994]. The NCEP surface albedo comes from a climatology [*Kanamitsu*, 1989; *Kalnay et al.*, 1996]: The current land albedo is from *Matthews* [1985] with modification if there is snow cover (0.75 is assumed poleward of 70° latitude for permanent snow and 0.60 is assumed equatorward of 70° if snow depth is at least 0.01 m), sea ice albedo ranges from 0.45−0.65 and 0.65−0.8 for snow free and snow covered, respectively, and open water albedo is solar zenith angle dependent but no specifics could be found. NCEP albedos do not depend on the spectral interval (see ftp://ftpprd.ncep.noaa.gov/pub/cpc/wd51we/reanal/random_notes/model). Since all of the above albedo models are relatively simple, we do not use them for this work.

[8] The NASA Global Energy and Water Cycle Experiment (GEWEX) Surface Radiation Budget (SRB) Project has developed a 12-year/148-month global data set for surface SW and LW fluxes on 1° × 1° grid, called SRB release 2 [*Stackhouse et al.*, 2001, 2004] (now extended to 22 yrs). The SW algorithm used for SRB is from *Pinker and Laszlo* [1992] in which land and ocean albedo values, as a function of solar zenith angle and wavelength, are clear-sky surface albedos based on *Briegleb et al.* [1986]. We call this version of albedo SRB-ALB.

[9] The NASA Goddard Institute for Space Studies (GISS) GCM Model II [*Hansen et al.*, 1983] uses a global, seasonally varying land surface albedo data set that was constructed by combining a land surface type/vegetation classification from the work of *Matthews* [1985] with field and laboratory albedo measurements for different rock, soil and vegetation types. Snow is treated as an added component that modifies the surface albedo accordingly. Both snow and ice albedos are also (implicitly) solar zenith angle dependent. The spectrally and solar zenith angle dependent ocean albedo is based on calculation of Fresnel reflection from a surface wave-slope distribution as a function of wind speed [*Cox and Munk*, 1956]. The 1983 version of the albedo values are for two wavelength ranges: visible (VIS) from 0.2 to 0.7 μm and near infrared (NIR) from 0.7 to 5.0 μm, together covering the whole solar spectrum. The revised 2001 (current) version of this product, which we will call GCM-ALB, has albedo values for six wavelength ranges: VIS and five covering the NIR. The revised ocean albedo includes the effects of foam and hydrosols. For all of the work using the GISS model, the default wind speed = 2 m/s (for a more detailed description, see *Zhang et al.* [2004]). The version used here for albedo values has a spatial resolution of 280 km and is "climatological" in that it represents no particular year (except for snow/ice areas).

[10] Based on the 1983 version of the GISS GCM, *Zhang et al.* [1995] produced a broadband albedo product by combining the surface visible albedo taken directly from visible reflectances (at wavelength about 0.6 μm) in the ISCCP cloud products [*Rossow and Garder*, 1993] and the

Table 1a. Comparison Between ISCCP6 and Surface Radiation Budget (SRB) for Monthly Mean Broadband Clear-Sky Surface Albedo for Snow-Free Land, Ice-Free Water, Snow-Covered Land, and Sea Ice for January, April, July, and October 1992[a]

	Snow-Free Land	Ice-Free Water	Snow-Covered Land	Sea Ice
9201	−1.7 (5.8)	−0.7 (1.9)	15.0 (11.4)	20.6 (16.8)
9204	−1.0 (4.5)	−0.3 (3.8)	10.9 (3.5)	7.5 (6.4)
9207	−3.4 (3.8)	−0.4 (4.4)	7.1 (4.8)	8.1 (3.8)
9210	−2.0 (4.4)	0.0 (2.1)	11.7 (6.3)	7.8 (6.1)
Mean	−2.0 (4.6)	−0.3 (3.0)	11.2 (6.5)	11.0 (8.3)

[a]Surface albedo is given in %. Sea ice is defined as >95% of a grid box through all the days of a month using ISCCP snow and ice data. Globally averaged mean difference (ISCCP6 minus SRB) with its spatial standard deviation in parentheses from 280-km equal-area maps. Last row shows the mean values of the above 4 months.

GCM's ratio of the NIR to visible albedo. The land-type-dependent visible albedo is replaced by a 3-year seasonal average of the ISCCP-C1 visible reflectances and the NIR albedos adjusted by regression with ERBE's TOA clear-sky SW fluxes to minimize systematic errors. This product has a spatial resolution of 280 km and represents albedo values for particular time periods (1985–1988). We refer to this data set as ISCCP2-ALB (where the "2" refers to the number of spectral bands).

[11] Similarly, we have produced an updated version of the previous product by employing the 5 spectral ratios of the 5 NIR wavelengths to visible albedo from the 2001 GISS GCM and the new ISCCP-D1 surface visible reflectances (now corrected for aerosols using a climatology). We refer to this data set as ISCCP6-ALB, which is used in our new radiative transfer flux product ISCCP-FD [*Zhang et al.*, 2004].

[12] The MODIS team (of Boston University) has produced a land surface albedo data set at several spatial resolutions (from 5 km) for 16-day periods since February 2000 based on a three-parameter semiempirical RossThick-LiSparse-Reciprocal (RTLSR) bidirectional reflectance distribution function (BRDF) model to characterize the anisotropic reflectivity of the land surface [*Jin et al.*, 2003a, 2003b]. In their albedo retrieval irradiance model (MODTRAN), twenty surface reflectance spectra, four visibility values for different aerosol loadings, five default aerosol models, twelve different water vapor profiles from the Tropical Ocean Global Atmosphere Coupled Ocean-Atmosphere Response Experiment project but with adjustments, and five types of default clouds (essentially some climatological atmosphere) are used [*Liang et al.*, 1999]. The snow/ice flag is turned on if the majority of observations are indicated as snow/ice during a 16 day period, and only those observations are used for BRDF and albedo snow inversion [*Schaaf et al.*, 2002]. The surface cover types are assumed Lambertian. In this study, we use a data set provided by Crystal B. Schaaf at http://duckwater.bu.edu/brdf_albedo/albedo16/params.htm from the original version 4 product (MOD43C2 V004 16-day L3 Global 0.05° CMG, as of 2004). The original BRDF parameters for 0.05° × 0.05° cells are used to calculate BSA for three wavelength ranges: visible (0.3–0.7 μm), NIR (0.7–5.0 μm) and total SW (0.3–5.0 μm) using a polynomial function of solar zenith angle (supplied by MODIS team, see *Lucht et*

al. [2000]) with a 16-day mean solar zenith angle (representing a 16-day period "mean" BSA). The fine-scale albedo values are then (linearly) averaged to our standard 280-km equal-area map grid cells when ≥90% of the 0.05° cells have values within a box. This albedo data set, called MODIS-ALB, is for land only. Using the formulae provided by the MODIS team, we have produced MODIS BSA for four 16-day periods (beginning dates are 6 April, 11 July, and 29 September 2000 and 17 January 2001) for comparison with matched values from ISCCP6-ALB for visible, NIR, and total SW BSA. In addition, the MODIS BRDF parameters for one 16-day period (11–24 July 2000, representing all of July) and two 16-day periods (1 January to 1 February 2001) are used to calculate 3-hourly surface visible and NIR BSA values for these two months that are then used in our current radiation model [*Zhang et al.*, 2004] in place of ISCCP6-ALB to calculate ISCCP-FD-like MODIS (thereafter, MODIS-FD) 3-hourly TOA/surface clear-sky albedos/fluxes for July 2000 and January 2001. The monthly means are compared with matching values from ISCCP-FD and the Clouds and the Earth's Radiant Energy System (CERES) ERBE-like data sets [*Wielicki et al.*, 1996; see also *Zhang et al.*, 2004].

[13] There are also various regional albedo products, e.g., the Meterosat Surface Albedo based on two adjacent geostationary satellites Meteosat-7 and 5 (currently operated by EUMETSAT). The production relies on a daily accumulation of the satellite observations acquired under more than fifteen different illumination conditions to assess the scattering properties of the surface and the atmosphere with some assumptions, and estimates the directional hemispherical reflectance values, for visible band ($\sim$0.5–0.9) that is corrected for atmospheric effects (i.e., BSA), which may be linearly related to broadband albedo. The product is planned for retrievals of albedo values for the whole Meteosat record (1982 to current) on a daily basis [*Govaerts et al.*, 2004].

2.1.2. Comparison of Broadband Albedos

[14] Table 1a shows the global mean (rms = rms with bias removed; this will be used for all rms values throughout the paper) of regional differences for monthly mean clear-sky surface albedo between ISCCP6-ALB and SRB-ALB for January, April, July, and October 1992, for four broad surface types: snow-free land, ice-free water, snow-covered land and sea ice, where snow/ice cells are defined by coverage ≥95% of a 280-km equal-area box on all the days of a month based on the ISCCP snow/ice data. The last row of the table summarizes the average results for the four seasonal months. In general, the two albedo sets are in good agreement for snow-free land and ice-free water: The mean (rms) differences (ISCCP6 minus SRB-ALB) are −2.0% (4.6%) and −0.3% (3.0%), respectively. However, for snow-covered land and sea ice, the differences become 11.2% (6.5%) and 11.0% (8.3%), respectively. We have also compared these products for seven representative vegetation types: (1) Amazon rainforest, (2) Sahara Desert, (3) snow-free grassland, (4) snow-free deciduous forests, (5) snow-covered grassland, (6) land ice (with or without snow), and (7) sea ice. These regions are defined in the same way as above except that the snow-free vegetated regions are defined by >66% coverage by the type of vegetation for a 280-km equal-area grid cell. Table 1b shows the comparison between ISCCP6-ALB and SRB-

Table 1b. Comparison Between ISCCP6 and SRB for Monthly Mean Broadband Clear-Sky Surface Albedo[a]

| Region Number | ISCCP6 (X) Mean | SRB (Y) Mean | X−Y Mean | Standard Deviation of (X−Y) | Regression | | | | Grid Box Number |
					Correlation Coefficient	Slope	Intercept	Nm Dev	
1	14.5	19.9	−5.4	1.9	0.714	1.4	0.1	0.8	160
2	32.8	29.9	2.9	4.3	0.766	0.8	3.6	3.0	484
3	15.2	16.2	−1.1	3.5	0.515	0.8	3.5	2.4	150
4	11.6	14.0	−2.4	3.1	0.607	0.9	3.6	2.2	277
5	54.5	44.0	10.5	4.9	0.973	0.8	4.8	2.5	33
6	76.6	73.2	3.4	2.6	−0.280	0.9	2.2	2.1	152
7	69.0	61.0	8.0	6.1	0.773	0.8	4.8	3.5	274

[a]Albedo is given in %. Collected from the four months (Table 1a) for seven regions. As numbered in column one, the seven types of land features (based on ISCCP surface information) are (1) Amazon rainforests, (2) Sahara Desert, (3) snow-free grassland, (4) snow-free deciduous forests, (5) snow-covered grassland, (6) land ice (with or without snow cover), and (7) sea ice. All surface features (other than vegetation types) are defined when such features >95% of a 280-km equal-area box, and all vegetation types are defined as they are >66% of a grid box. "Nm Dev" is the RMS distance of all points from the regression line.

ALB for the four monthly mean clear-sky albedos for the seven surface types. The largest biases (magnitude ≥5%) appear in Amazon rainforests, snow-covered grassland, and sea ice: Albedo values are more difficult to determine in these regions because of contamination by persistent clouds and snow.

[15] Table 1c compares surface BSA for visible, NIR and total broadband SW between ISCCP6-ALB and MODIS-ALB for the four (seasonal) 16-day periods for snow-free land (defined by both snow maps being snow free), snow-covered land (both maps have grid cells with ≥ 75% snow) and all land (all available cells for both). For snow-free land, there is a good agreement in the visible band: Mean (rms) regional differences (FD minus MODIS) are 0.9% (3.5%). Disagreement in the NIR is much greater: Mean (rms) regional differences are −19% (6.7%). The MODIS retrieval algorithm has larger errors in the NIR than in the visible [*Jin et al.*, 2003a] because the radiances are smaller and the atmospheric absorption is much stronger. On the other hand, the NIR albedo values in ISCCP6-ALB rely on a surface-classification-based GCM model, which is a long-term climatological surface representation based on

Matthews [1985], but adjusted by regression with ERBE to reduce systematic errors. There is not sufficient evidence to decide which of these NIR results is better than the other (see next paragraph). For snow-covered land, both the agreement and disagreement are smeared out and their mean (rms) regional differences become −3% (14%) and −6.8% (10%) for visible and NIR, respectively.

[16] The visual comparison for the seven representative vegetation types is shown in Figure 1. Figures 1a to 1c are scatterplots between ISCCP6 (= X) and MODIS (= Y) BSA for Amazon rainforests, snow-free grassland and snow-free deciduous forests for visible, NIR and total SW, respectively, for the same four 16-day periods (on 280-km equal-area map), and Figures 1d to 1f are their counterparts for snow-covered grassland, land ice, sea ice, and Sahara Desert. Because of sparse sampling in MODIS, there are only 7 and 6 grid cells with available albedo values from all the four periods for land ice and sea ice, and as a result, their comparisons are statistically insignificant. For the other five regions, generally speaking, the figures are more or less different from the mean comparison results shown in Table 1c. The Sahara Desert and snow-covered grasslands

Table 1c. Comparison Between ISCCP6 and MODIS for 16-day Mean Visible, Near-Infrared (NIR), and Total Shortwave (SW) Broadband Black-Sky Land Surface Albedo[a]

| Band | ISCCP6 (X) Mean | MODIS (Y) Mean | X−Y Mean | Standard Deviation of (X−Y) | Regression | | | | Grid Box Number |
					Correlation Coefficient	Slope	Intercept	Nm Dev	
			(1) Snow-Free Land (When Both are Snow-Free)						
Visible	11.9	11.0	0.87	3.53	0.9093	0.995	−0.81	2.50	3842
NIR	11.8	30.9	−19.12	6.69	0.7831	0.998	19.14	4.74	3842
Total SW	11.9	21.0	−9.13	4.32	0.8771	0.993	9.21	3.07	3842
			(2) Snow-Covered Land (When Both Snow ≥75%)						
Visible	44.3	47.3	−2.99	14.25	0.8584	0.995	3.22	10.11	1137
NIR	31.4	38.2	−6.81	10.09	0.7626	0.742	14.91	7.50	1137
Total SW	38.5	42.7	−4.18	11.63	0.8400	0.902	7.95	8.52	1137
			(3) All Land (When Both Data are Available)						
Visible	18.3	18.0	0.31	7.51	0.9318	1.058	−1.37	5.11	5958
NIR	15.6	31.4	−15.74	9.05	0.7259	0.683	20.69	6.71	5958
Total SW	17.2	24.7	−7.55	6.96	0.8957	0.880	9.61	5.04	5958

[a]Given in % from four 16-day periods (see text) for (1) snow-free land, (2) snow-covered land (defined as both are snow free and ≥75% snow of a cell), and (3) all land on 280-km equal-area maps.
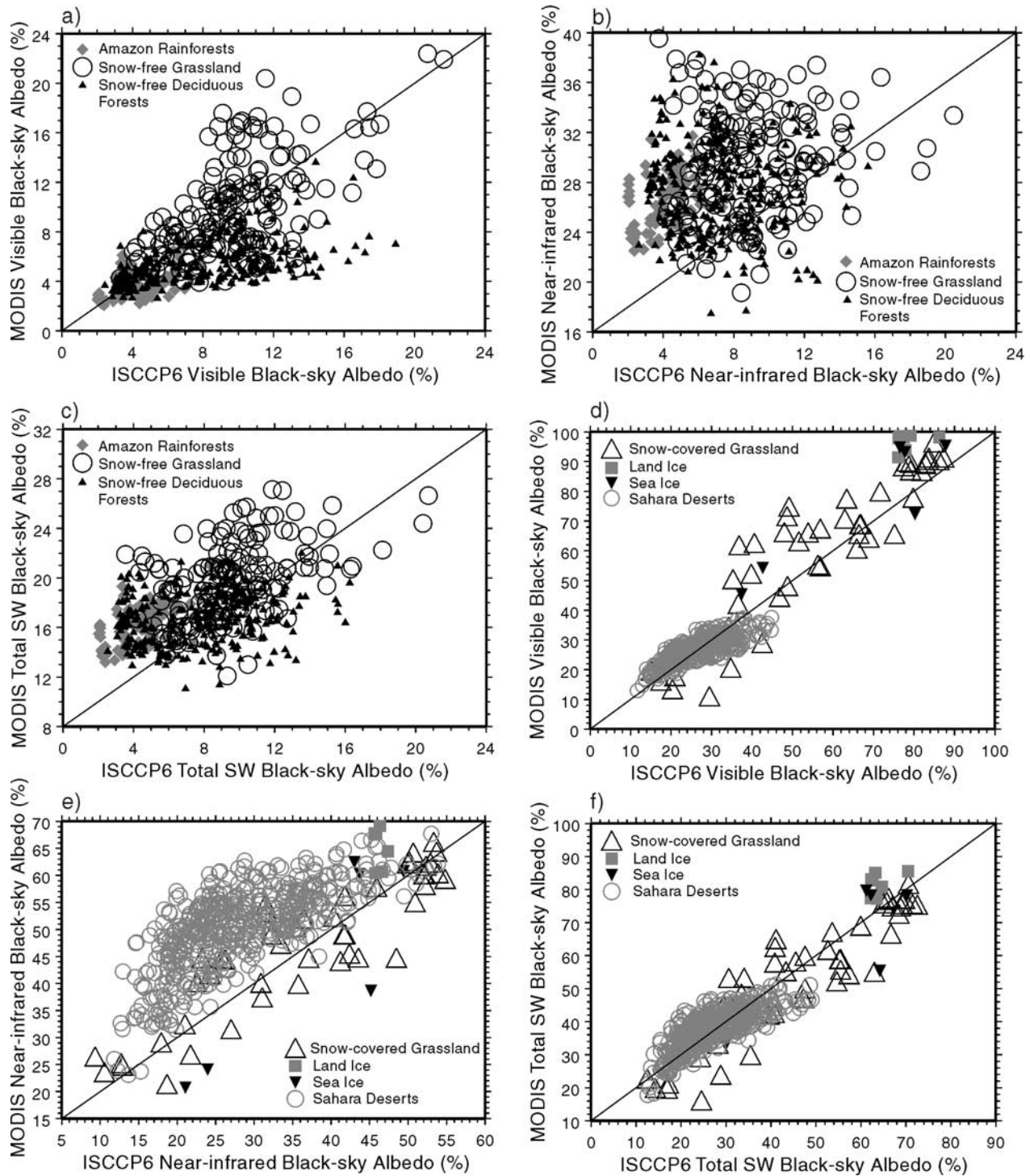
Figure 1. (a) Scatterplot of visible black-sky albedo (in %) for Amazon rainforests (dark grey diamonds), snow-free grassland (open circles), and snow-free deciduous forests (solid triangles) from ISCCP6 and MODIS for four 16-day periods (beginning on 6 April, 11 July, and 29 September 2000 and 17 January 2001). (b) Same as in Figure 1a but for near infrared, and the diagonal line is not plotted from the origin (0,0), but from the point that visually approximately reflect their mean bias for all the corresponding regions. (c) Same as in Figure 1b but for total shortwave (SW) (visible and near infrared). (d) Scatterplot of visible black-sky albedo (in %) for snow-covered grassland (open triangles), land ice (dark grey squares), sea ice (solid triangles), and Sahara Desert (dark grey diamonds) from ISCCP6 and MODIS for four 16-day periods (beginning on 6 April, 11 July, and 29 September 2000 and 17 January 2001). (e) Same as in Figure 1d but for near-infrared, and the diagonal line is not plotted from the origin (0,0), but from the point that visually approximately reflect their mean bias for all the corresponding regions. (f) Same as in Figure 1e but for total SW (visible and near-infrared).
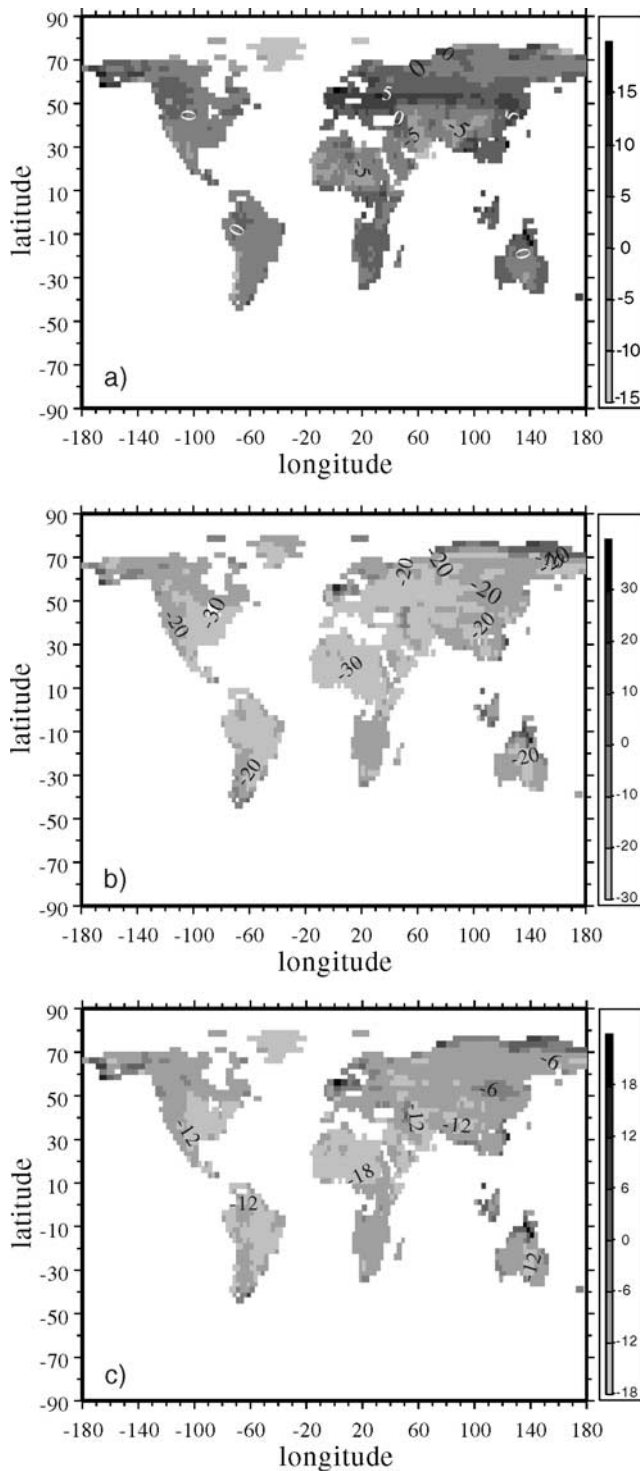
Figure 2. (a) Global map of differences (ISCCP6 minus MODIS) of visible black-sky albedo (in %) from four 16-day periods (beginning on 6 April, 11 July, and 29 September 2000 and 17 January 2001). (b) Same as in Figure 2a but for near-infrared. (c) Same as in Figure 2a but for total SW (visible and near-infrared).

have the highest correlations (>0.71) for all the three bands, but large mean differences always appear in NIR (−22% and −10% in ISCCP6 minus MODIS, respectively). The least agreement appears in Amazon forests (correlation

coefficients are 0.46 and 0.41 for visible and NIR, respectively, while their mean differences are 0.7% and −22%, respectively). Also, ISCCP6 and MODIS have better agreement in visible band than in NIR band as also shown in Table 1c.

[17] To obtain a global picture, Figures 2a to 2c show the global maps of the BSA differences (ISCCP6 minus MODIS) for visible, NIR, and total SW, respectively, for the 16-day period of 11 July (beginning date). Again, the visible map shows that, for the majority of the world, the two data set differ only within ±5% (mean global difference = −0.5%). The largest discrepancy (up to −35% difference) appears in central Greenland (where MODIS has less data), possibly because of the difficulty of identifying clear conditions over such bright regions. There is a narrow belt from England to the northeast China for essentially intensively cultivated lands [*Matthews*, 1982] where ISCCP6 is 5–10% higher than MODIS. The NIR map shows large difference (mean global difference = −20%) and systematical regional pattern dependence, indicating the two data sets have some fundamental difference in deriving the NIR albedos. The most prominent region is the North African deserts, where ISCCP6 is less than MODIS by >30%. For the total broadband SW, the majority of land areas show a difference around −10% (also the global mean difference).

[18] Table 1d shows the comparison of calculated monthly mean surface clear-sky (apparent) albedo and upward SW between ISCCP-FD and MODIS-FD for snow-free, snow-covered and total land. The agreement between ISCCP-FD and MODIS-FD is very good showing that the large NIR BSA differences have far less effect on the total clear-sky (apparent) albedo and upwelling SW fluxes because the atmosphere absorbs most of the SW radiation in the NIR band. For all land, the mean (rms) regional differences between ISCCP and MODIS are only 0.14% (7%) and −2.5 (11) Wm^{-2} for the albedo and upwelling SW, respectively.

[19] Tables 2a and 2b show the comparisons of ERBE TOA clear-sky albedo with ISCCP-FD and SRB, respectively, for the four seasonal monthly means of 1986 when ERBE data is available. For snow- and ice-free lands, both TOA clear-sky albedos are in good agreement with ERBE: ISCCP is within 1% bias while SRB is within 2 %. This is not the case for snow-covered grassland, land and sea ice (land types 5 through 7), where ISCCP-FD exhibits a bias up to about 8% while the SRB bias is up to 13%. For snow-covered grassland (type 5), ISCCP-FD is biased high while SRB is biased low; but for land and sea ice, both ISCCP-FD and SRB are biased low. The reasons may lie partly in their fundamentally different analysis approaches and partly in the cloud contamination for ERBE. One known problem for the high-latitude results in SRB, which uses the ERBE angle models to determine fluxes from radiances [*Pinker and Laszlo*, 1992], is that these angle models are biased for large solar zenith angles [*Suttles et al.*, 1992].

[20] Although ISCCP-FD and MODIS have mean regional differences of −7.6% for surface BSA (based on four 16-day periods and all land areas), these differences produce TOA clear-sky albedo mean (rms) differences of only −0.31% (3.4%) (not shown) because TOA albedo is insen-

Table 1d. Comparison of Monthly Mean Surface Clear-Sky Albedo (%) and Upwelling SW Flux (W/m^{-2}) Between ISCCP-FD and MODIS-FD[a]

Clear Sky	FD (X) Mean	MODIS-FD (Y) Mean	X−Y Mean	Standard Deviation of (X−Y)	Correlation Coefficient	Slope	Intercept	Nm Dev	Grid Box Number
					Regression				
				(1) Snow-Free Land (When Both Are Snow Free)					
Albedo	14.4	15.7	−1.33	3.50	0.9287	0.868	3.23	2.47	1981
SW-up	40.4	44.3	−3.87	10.13	0.9218	0.934	6.56	7.30	1981
				(2) Snow-Covered Land (When Both Snow ≥75%)					
Albedo	49.5	45.2	4.32	13.26	0.8166	0.800	5.56	9.76	568
SW-up	74.1	74.5	−0.69	12.51	0.9941	1.052	−3.15	7.85	568
				(3) All Land (When Both Data Are Available)					
Albedo	21.1	21.0	0.14	7.12	0.9249	0.832	3.41	4.91	3002
SW-up	46.4	48.9	−2.51	11.09	0.9775	1.017	1.70	7.75	3002

[a]See text; given for collective July 2000 and January 2001 monthly means for (1) snow-free land, (2) snow-covered land, and (3) all land on 280-km equal-area maps.

sitive to surface NIR albedo, the visible band contributing most to the SW fluxes at TOA. Tables 2c and 2d compare monthly mean TOA clear-sky albedos from CERES (ERBE-like) with those from ISCCP-FD and MODIS-FD, respectively, for July 2000 and January 2001. The bias of ISCCP-FD with respect to CERES (−0.29%) is slightly smaller than for MODIS-FD (0.70%) for snow-free land, but the rms difference is slightly larger (2.4%) than for MODIS (1.7%). For snow-covered land, ISCCP has a larger bias (4.6%) and rms difference (11%) than MODIS (3.0%, 9.8%). For all land, ISCCP-FD and MODIS have biases (rms) = 0.90% (5.7%) and 1.2% (4.5%), respectively. Both albedo products produce good agreement with the CERES albedos on average but ISCCP exhibits more scatter relative to CERES than MODIS does. These statistics do not provide strong evidence for choosing between these two albedo products. Figure 3 shows the scatterplots of TOA clear-sky upward SW fluxes from CERES against the results from ISCCP-FD and MODIS-FD for snow-free and snow-covered land areas. From Figures 3a and 3b (snow-free land) we see that MODIS appears to perform slightly better than ISCCP: The points off the diagonal (>110 Wm^{-2}) in Figure 3a are located in Northern Africa and the Arabian Peninsula, where ISCCP is biased low. The fact that the pattern of disagreement for snow-covered land shown in Figures 3c and 3d is the same for both ISCCP-FD and MODIS-FD suggests that this disagreement might be partly caused by the ERBE angle models for this surface type.

[21] Table 3a (for snow-free land and ice-free ocean) and 3b (for snow-covered land and sea ice) compare TOA albedo and upwelling SW fluxes for clear-sky scenes with ERBE for ISCCP2-ALB, GCM-ALB, ISCCP6-ALB and SRB-ALB. The albedo and fluxes are calculated from their corresponding surface broadband BSA or clear-sky albedo, whichever applies. From the first three entries, we can see that adjusting the GCM albedo using the ISCCP visible reflectances for land improved the albedo/flux comparison substantially. Going to six wavelength ranges also provides some overall improvement over the original two-wavelength range treatment. For snow-free land and ice-free water regions, the SRB-ALB results are comparable with ISCCP6-ALB; that is, both have a good agreement with ERBE, but for snow-covered land and sea ice regions, SRB-ALB has a larger bias than ISCCP6-ALB. There are three notable conclusions. First, except for GCM-ALB, all of the other products are adjusted to agree with ERBE in some way, yet the remaining regional scatter in surface albedo for snow-free land or ice-free water is still several percent, and even larger for snow/ice surfaces. Second, although the reconstruction of surface albedo from a surface vegetation/land use classification produces a fairly accurate result as shown for NASA GISS GCM model (which can be compared with other major GCM results), use of the ISCCP visible reflectance data improves the result, which implies that there is significant regional (and temporal) variation in the albedo of surfaces with the same classification [cf. *Matthews and Rossow*, 1987]. Third, it is still possible to improve surface albedo maps by producing and using better satellite-based surface albedo data sets. We note that MODIS is the first imaging instrument to provide measurements at wavelengths covering the whole solar spectrum.

Table 2a. Same as in Table 1b but Comparing ISCCP-FD and Earth Radiation Budget Experiment (ERBE) for Broadband Top of the Atmosphere (TOA) Clear-Sky Albedo (in %) Collected From Monthly Means for January, April, July, and October 1986

Region Number	ISCCP-FD (X) Mean	ERBE (Y) Mean	X−Y Mean	Standard Deviation of (X−Y)	Correlation Coefficient	Slope	Intercept	Nm Dev	Grid Box Number
					Regression				
1	14.5	15.6	−1.1	1.4	0.386	1.0	1.5	2.4	124
2	31.3	32.3	−1.0	2.2	0.866	1.0	1.3	1.5	484
3	18.4	19.2	−0.8	3.0	0.450	1.0	1.8	1.7	150
4	18.0	17.6	0.4	3.2	0.241	1.0	−0.1	2.0	272
5	43.0	40.1	2.9	12.9	0.740	1.0	0.4	3.3	40
6	65.7	73.5	−7.8	2.5	0.032	1.1	−2.4	1.8	148
7	57.8	63.3	−5.5	6.3	0.447	1.1	−1.5	2.8	133

Table 2b. Same as in Table 2a but for SRB and ERBE

Region Number	SRB (X) Mean	ERBE (Y) Mean	X−Y Mean	Standard Deviation of (X−Y)	Regression Correlation Coefficient	Slope	Intercept	Nm Dev	Grid Box Number
1	17.6	15.6	2.0	1.3	0.339	1.2	−4.2	2.0	124
2	30.0	32.3	−2.2	2.5	0.821	1.0	2.0	1.8	484
3	19.3	19.2	0.0	2.6	0.309	1.0	0.7	1.7	150
4	18.0	17.6	0.4	2.5	0.129	1.0	−0.5	1.7	272
5	36.5	40.1	−3.7	13.0	0.766	1.1	−2.1	2.9	40
6	60.2	73.4	−13.2	2.1	0.512	1.3	−5.2	1.9	144
7	52.5	61.4	−8.9	7.0	0.204	1.2	−3.1	2.8	110

[22] Figure 4 shows the zonal mean TOA clear-sky albedo from ISCCP6-ALB (from ISCCP-FD), SRB-ALB and ERBE for July 1986 and January 1987. In most zones, the former two are comparable and exhibit biases with ERBE ≤ 5% or so. In the winter hemispheres, at about 40°−55°S for July and 30°−45°N for January, SRB performs better than ISCCP-FD, while in summer hemispheres, ISCCP usually performs better than SRB. In the polar regions, ISCCP-FD values are closer (especially in January) to ERBE than SRB.

2.2. Infrared Emissivity

2.2.1. Data Sets

[23] Infrared emission from the surface depends on both temperature, which varies rapidly in time especially for land, and emissivity that varies with wavelength and surface properties in a complex way. Emissivity also plays an important role in determining surface temperature by remote sensing [e.g., *Becker*, 1987]. Because the thermal (LW) emissivity at the Earth's surface is close to unity, most applications assume it to be unity [*Peixoto and Oort*, 1992], which is also the case given by *Zhang et al.* [1995]. As a result, there were no high-quality global surface emissivity data sets determined from satellite observations (3I produces emissivity at 50 Ghz, see also *Prigent et al.* [1997, 2000], but not for thermal radiation spectral range) or otherwise at the start of this work. The only global databases for this surface property (in terms of LW flux calculation) are constructed by combining field and laboratory measurements of the emissivities of various rock, soil and vegetation types, which are generally only measured for

wavelengths <20 μm, with a surface classifications and theoretical calculations (especially for water as in the GISS climate model, where the emissivity = 1 − albedo and the albedo is calculated using Fresnel reflection as explained before).

[24] Since July 2001, there have appeared several versions (still kept updating) of the MODIS-based high-spatial-resolution Land Surface Temperature product that also includes emissivity, which is for 6 wavelength bands, ranging from 3.66 to 12.17 μm [see, e.g., *Wan et al.*, 2004]. Because this product is only for several narrow bands and still being validated, we do not used it in this study.

[25] Two versions data sets are examined here, one from the GISS GCM and used in ISCCP-FD with a spatial resolution of 280 km and emissivity values in 33 k-intervals covering the whole LW range (5−200 μm) [cf. *Lacis and Oinas*, 1991] and one adopted from *Wilber et al.* [1999], used for the determination of surface radiative fluxes by the SRB and CERES with the Fu-Liou radiative transfer code [*Fu and Liou*, 1992]. In deriving the broadband emissivity (5.0−100 μm), *Wilber et al.* [1999] used laboratory measurements for nine materials (including water) over a wavelength range of 4−16 μm and, by averaging 12 Fu-Liou band values (covering 4.5 − ∞ μm) weighted by the Planck function energy distribution, extrapolated them to broadband emissivities for 18 surface types (including water), representing all the possible surface types. The global broadband emissivity (for nadir viewing conditions) is then constructed based on the 18 types on a 10′ × 10′ global grid, which we regridded to 280-km equal-

Table 2c. Comparison Between ISCCP-FD and CERES for Monthly Mean TOA Clear-Sky Albedo Collected From July 2000 and January 2001[a]

ISCCP-FD (X) Mean	CERES (Y) Mean	X−Y Mean	Standard Deviation of (X−Y)	Regression Correlation Coefficient	Slope	Intercept	Nm Dev	Grid Box Number
(1) Snow-Free Land								
18.1	18.4	−0.29	2.38	0.9231	0.913	1.87	1.71	1978
(2) Snow-Covered Land								
44.7	40.0	4.64	11.34	0.8082	1.084	−8.42	7.65	486
(3) All Land								
22.8	21.9	0.90	5.70	0.8972	0.880	1.84	4.12	2916

[a]Snow maps are from FD and MODIS only.

Table 2d. Same as in Table 2c but for MODIS-FD and CERES

MODIS-FD (X) Mean	CERES (Y) Mean	X−Y Mean	Standard Deviation of (X−Y)	Regression				Grid Box Number
				Correlation Coefficient	Slope	Intercept	Nm Dev	
(1) Snow-Free Land								
19.1	18.4	0.70	1.65	0.9616	1.009	−0.87	1.16	1978
(2) Snow-Covered Land								
43.0	40.0	2.97	9.76	0.8703	1.175	−10.52	6.11	486
(3) All Land								
23.1	21.9	1.21	4.50	0.9323	0.988	−0.94	3.20	2916

area map for our comparison. We refer to these two data sets as GCM-EMIS and SRB-EMIS. In the process, *Wilber et al.* [1999] have also derived the 12 Fu-Liou band-average emissivities as well as CERES window (8–12 μm) emissivities for the 18 surface types.

[26] The ISCCP data set retrieves land surface brightness temperatures (with emissivity assumed to be unity) from infrared radiances measured at $\approx$11 μm wavelength in cloud-free scenes and corrected for atmospheric emission/absorption [cf. *Rossow and Garder*, 1993]. If accurate values of the land surface infrared emissivities at 11 μm
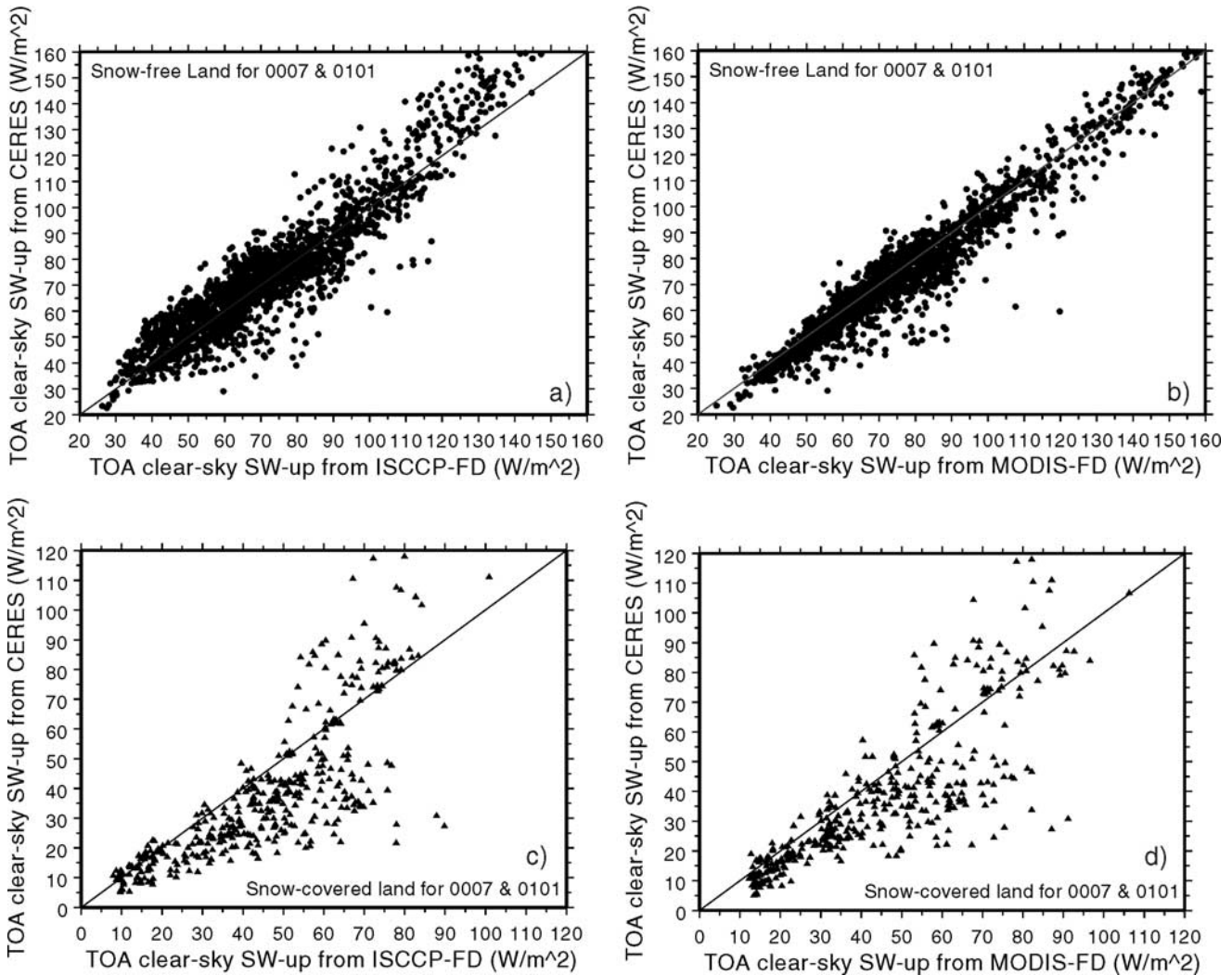

Figure 3. (a) Scatterplot of monthly mean top of the atmosphere (TOA) clear-sky SW-up fluxes (in W/m^2) for snow-free land from ISCCP-FD and CERES, accumulated from January and July 1992. (b) Same as in Figure 3a but for MODIS-FD and CERES. (c) Same as in Figure 3a but for snow-covered land. (d) Same as in Figure 3b but for snow-covered land.

Table 3a. Comparison of Monthly Mean Clear-Sky Broadband Planetary Albedo (in %) and Clear-Sky TOA Upwelling SW Flux (in W/m^2) Between the Results From Four Different Radiative Transfer Models With Their Own Surface Albedos (ISCCP2-ALB, GCM-ALB, ISCCP6-ALB and SRB-ALB) as Well as Other Inputs and the ERBE Results for July 1986 and January 1987[a]

	Snow-Free Land (≥95 %)				Ice-Free Water (≥95 %)			
	Clear-Sky TOA Albedo		Clear-Sky TOA SW-Up		Clear-Sky TOA Albedo		Clear-Sky TOA SW-Up	
Models Compared With ERBE	8607	8701	8607	8701	8607	8701	8607	8701
ISCCP2	1.3 (2.6)	1.0 (2.2)	5.1 (10.7)	3.5 (7.6)	1.4 (1.5)	1.1 (1.5)	4.2 (4.1)	3.8 (4.5)
GCM	4.2 (5.0)	4.2 (6.1)	16.4 (18.4)	16.4 (26.2)	1.6 (2.3)	0.3 (2.1)	3.2 (3.9)	−0.5 (4.8)
ISCCP6	−0.4 (2.4)	−0.9 (2.1)	−1.9 (10.1)	−3.8 (7.7)	1.5 (2.3)	0.3 (2.2)	3.1 (4.1)	−0.4 (5.6)
SRB	1.3 (3.1)	0.7 (3.1)	4.8 (12.7)	3.5 (11.3)	0.7 (2.1)	0.1 (2.0)	1.9 (6.1)	0.1 (7.9)

[a]The statistical numbers are globally averaged mean differences (all minus ERBE) with their corresponding spatial standard deviations in parentheses. The radiation models used to produce the results are old NASA GISS GCM (as ISCCP2 [see *Zhang et al.*, 1995]), current GISS model (as GCM), revised current GISS model (as ISCCP6 = 03-model [*Zhang et al.*, 2004]), and WCRP/GEWEX SRB model (release 2) (as SRB [see *Stackhouse et al.*, 1999]). Their main input data sets are ISCCP-C1 for ISCCP2, and ISCCP-D1 for the rest of the three models. Snow-free land and ice-free ocean areas are separated, defined as such surface features are ≥95% of a 2.5° equal-area box through all the days of a month using ISCCP6.

are available, these data can be corrected to estimate surface skin temperatures (T$_s$). Hence we also consider the available information about the "narrowband (11 μm)" or window region infrared emissivity. The version considered here also comes from the GISS GCM database (11.1−11.3 μm) and is compared with the CERES emissivity (8−12 μm).

2.2.2. Comparison of Broadband Emissivities

[27] Figure 5 shows a map of the differences of broadband emissivities between GCM-EMIS and SRB-EMIS. Values over land generally agree to within ±2%, but the coherent features exhibited in the figure suggest regional differences in classification. The GCM-EMIS values tend to be somewhat larger than the SRB-EMIS values for denser vegetation types (e.g., rainforests) and for some heavily cultivated locations (e.g., Europe and China, but not in southern Africa), and somewhat smaller than SRB-EMIS for intermediate density grasslands (e.g., the Russian steppes, central US) and most of middle/southern Africa (from dense forest to grass savanna), for mountainous terrains and even smaller in frozen areas (e.g., Greenland and Antarctic).

[28] Surprisingly, the largest differences are for open water (and ice/snow), ranging up to 7%. The SRB water emissivity neglects not only the strong spectral dependence (since its broadband emissivity is extrapolated from 12-band averages over 4−16 μm (weighted with the Planck function energy distribution)), but also zenith angle variations and wind speed effects. Averaging over all zenith angles produces an emissivity, even at "window" infrared wavelengths that is lower than the nadir value (usually measured in a laboratory). Wind roughening of the surface is equivalent to redistributing the zenith angles, but this has only a weak effect on the angle-averaged emissivity. For a

calm ocean surface, the emissivity (actually the reflectivity) can be accurately calculated using the Fresnel reflection formula [e.g., *Liou*, 2002], and under windy conditions, such calculations can be done with sufficiently high precision using a wave-slope distribution model as used in the GISS model. Figure 6a illustrates the variations of the GISS GCM emissivity values for water at wavelengths from 0.2 to 200 μm and surface wind speed = 3 m/s for cosine zenith angles 0.1, 0.5, and 1.0, and Figure 6b shows the emissivities at cosine zenith angle = 0.5 for wind speed = 3 and 7 m/s (Jacek Chowdhary, personal communication, 2005). From Figure 6a we see that the spectral difference in emissivity can be >15% and the extrapolation of SRB's emissivity to wavelengths beyond 16 μm tends to overestimate the broadband emissivity (5−100 μm as obtained by *Wilber et al.* [1999]).

[29] The difference of snow/ice surface emissivity comes from the use of different laboratory measurements for the GCM-EMIS and SRB-EMIS, the former adopted laboratory results from a variety of sources while the latter is basically from *Salisbury and D'Aria* [1992].

2.2.3. Comparison of Spectral Emissivities

[30] To convert the ISCCP surface (skin) brightness temperatures into physical temperatures, we use the narrowband emissivity at about 11 μm wavelength (see discussion about the trade off between correcting temperature and correcting emissivities in the work of *Zhang et al.* [2004]). Figure 7 shows the global difference map between the GCM-EMIS and SRB-EMIS narrowband values. Here the ocean values are in very good agreement while land and snow/ice locations generally agree within ±3%. The largest disagreements occur over arid and mountainous locations, including tundra: In all of these regions the GCM-EMIS

Table 3b. Same as in Table 3a, Except for Snow-Covered Land and Sea Ice

|	Snow-Covered Land (≥ 95 %)				Sea Ice (≥ 95 %)			
	Clear-Sky TOA Albedo		Clear-Sky TOA SW-Up		Clear-Sky TOA Albedo		Clear-Sky TOA SW-Up	
Models Compared With ERBE	8607	8701	8607	8701	8607	8701	8607	8701
ISCCP2	−2.4 (14.6)	−3.9 (9.5)	−11.4 (68.5)	−2.1 (10.8)	−8.4 (1.0)	N/A	−30.4 (18.4)	0.0 (0.3)
GCM	14.5 (10.0)	−10.4 (13.1)	68.4 (47.0)	−5.6 (16.0)	−12.5 (2.0)	N/A	−44.7 (27.8)	−0.1 (0.7)
ISCCP6	−1.2 (14.0)	−2.6 (9.1)	−5.8 (66.0)	−1.0 (10.3)	−2.7 (0.9)	N/A	−10.4 (6.9)	−0.1 (0.5)
SRB	−4.2 (14.4)	−14.3 (9.9)	−20.4 (67.5)	−11.2 (10.4)	−5.4 (0.9)	N/A	−21.1 (11.6)	−0.2 (1.7)
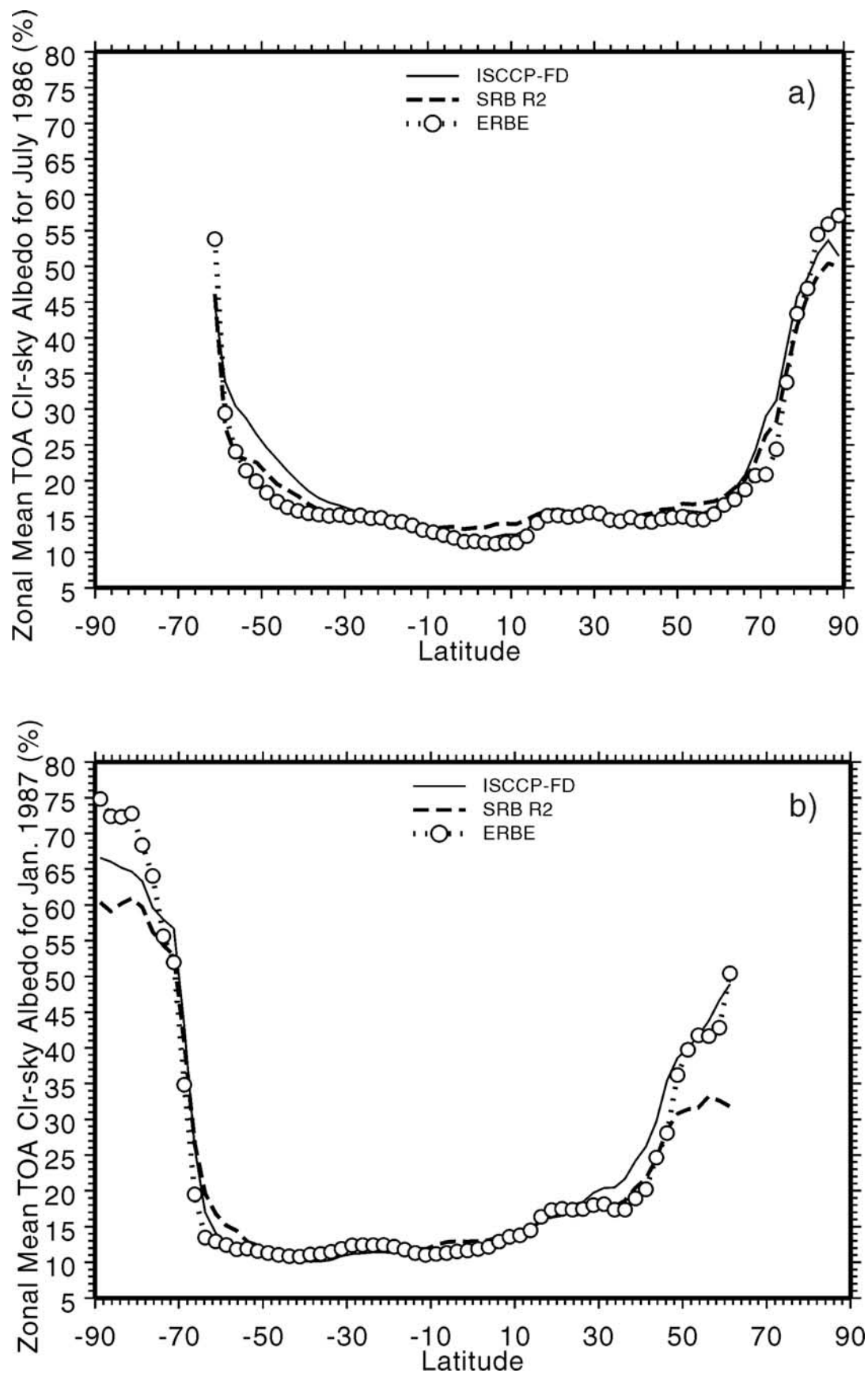
Figure 4. (a) Comparison of zonal monthly mean TOA clear-sky albedo (in %) from ISCCP-FD, surface radiation budget (SRB), and Earth radiation budget experiment (ERBE) for July 1986. (b) Same as in Figure 4a but for January 1987.
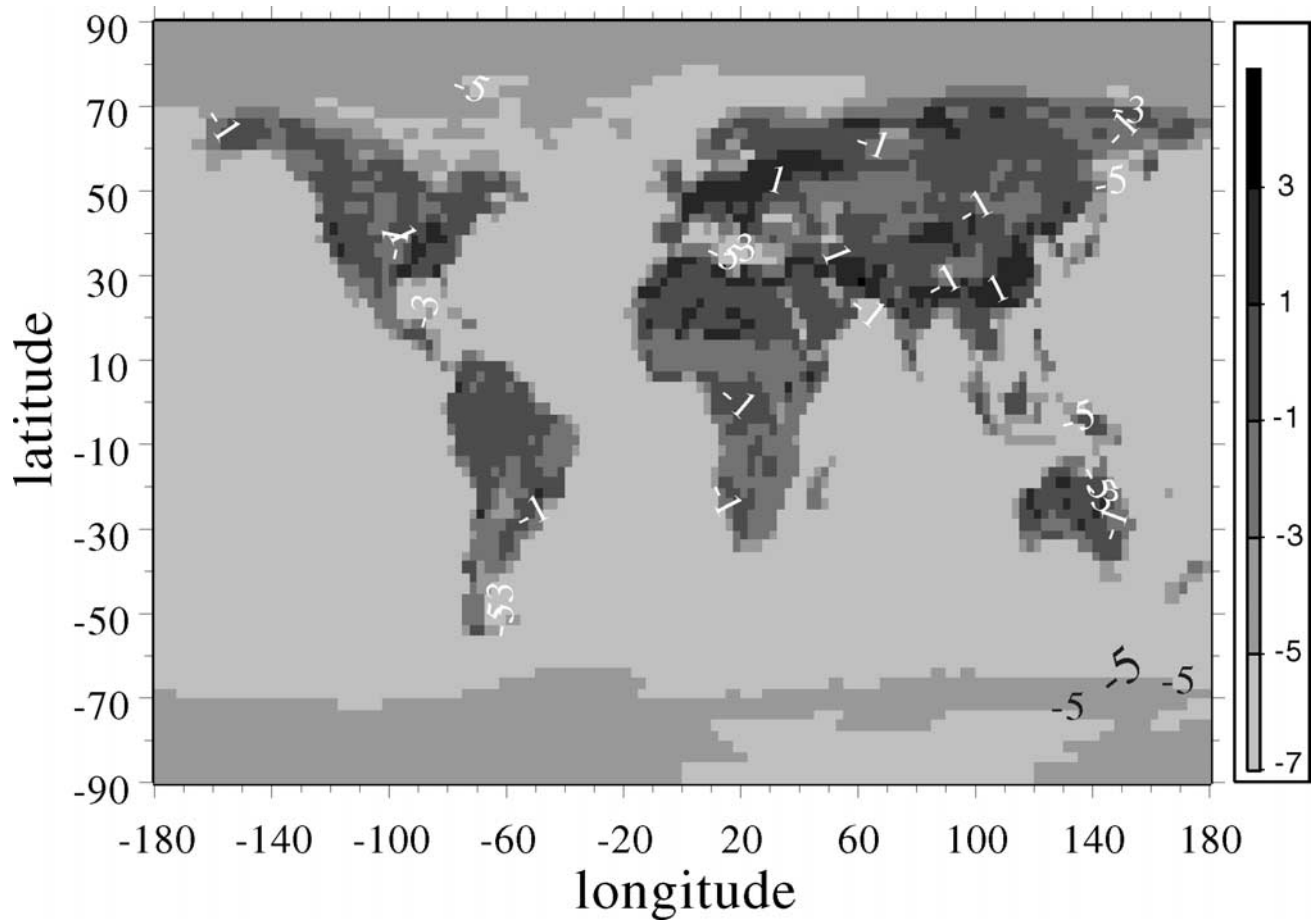
Figure 5. Global map of differences (ISCCP-FD minus SRB) of broadband emissivities (in %) from ISCCP-FD 1992 annual mean and SRB climatology.

values are significantly larger (>10%) than SRB-EMIS. Examining the reported values in detail suggests that the latter data set employs values consistent with bare rock and soil in these regions, whereas the former assumes some effect of sparse vegetation for most of these regions. The narrowband emissivity displays similar dependence on zenith angle as shown in Figure 6a but the surface wind speed dependence is much weaker. To correct the ISCCP surface temperature retrievals, which are made predominantly at small zenith angles (the average value is less than about 30°), we use a single value (0.985), a mean wind speed of 2 ms^{-1} and a simple approximation of the latitudinal dependence of reflected downwelling radiation for ISCCP-FD calculations [*Zhang et al.*, 2004]. In our sensitivity tests [see also *Zhang et al.*, 2004], if wind speed changes from 2 to 10 ms^{-1}, the emissivity change would induce a upwelling LW flux mean (rms) change by 0.5 (0.3) W/m^2 for global ocean, while a ±2% change (i.e., 4% of change) of emissivity would induce 2.1 (1.3) W/m^2 change for the whole globe.

2.3. Comparison of Surface Skin Temperatures

[31] All the major data sets have an associated surface skin temperature (T$_s$) as shown by *Zhang et al.* [2006, Table 1], but the values from FDTV and 3I are retrieved from satellite radiances using their respective temperature/

humidity profiles (the original FDTV, i.e., ISCCP-TOVS, T$_s$ values come from the ISCCP analysis that combines infrared radiances from imaging radiometers with the TOVS atmospheric profiles, whereas 3I uses the "window" channel radiances that are part of the temperature/humidity profile retrieval) and the other three are determined by the assimilation model as explained by *Zhang et al.* [2006, section 2.1].

[32] Comparison of the monthly mean T$_s$ maps from the five data sets (ERA15, GEOS-1, NCEP, 3I and FDTV) for the four seasonal months shows strongly similar pictures with spatial correlation coefficients for all possible pairs ≳0.95 (0.980 overall). Ocean areas are better correlated (0.986) than land areas (0.975). The largest regional differences, >40 and 35 K for land and ocean, respectively, between FDTV and GEOS-1, occur in the polar regions. Table 4 shows the global mean (rms) regional differences of T$_s$ for all ten pairs (ocean and land separately). The largest difference appears in (GEOS-1 minus FDTV) for land in January 1992: Mean (rms) difference = −4.7 (8.6) K. The overall modulus mean difference (i.e., absolute values of the mean differences, not affected by subtraction order, see e.g., *Reynolds* [1988]) (rms difference) is 0.52 (3.3) K (Table 4, footnotes), very similar to the modulus mean (rms) difference for surface air temperature T$_a$, 0.53 (2.6) by *Zhang et al.* [2006]. Like T$_a$, the global bias arises from a partial
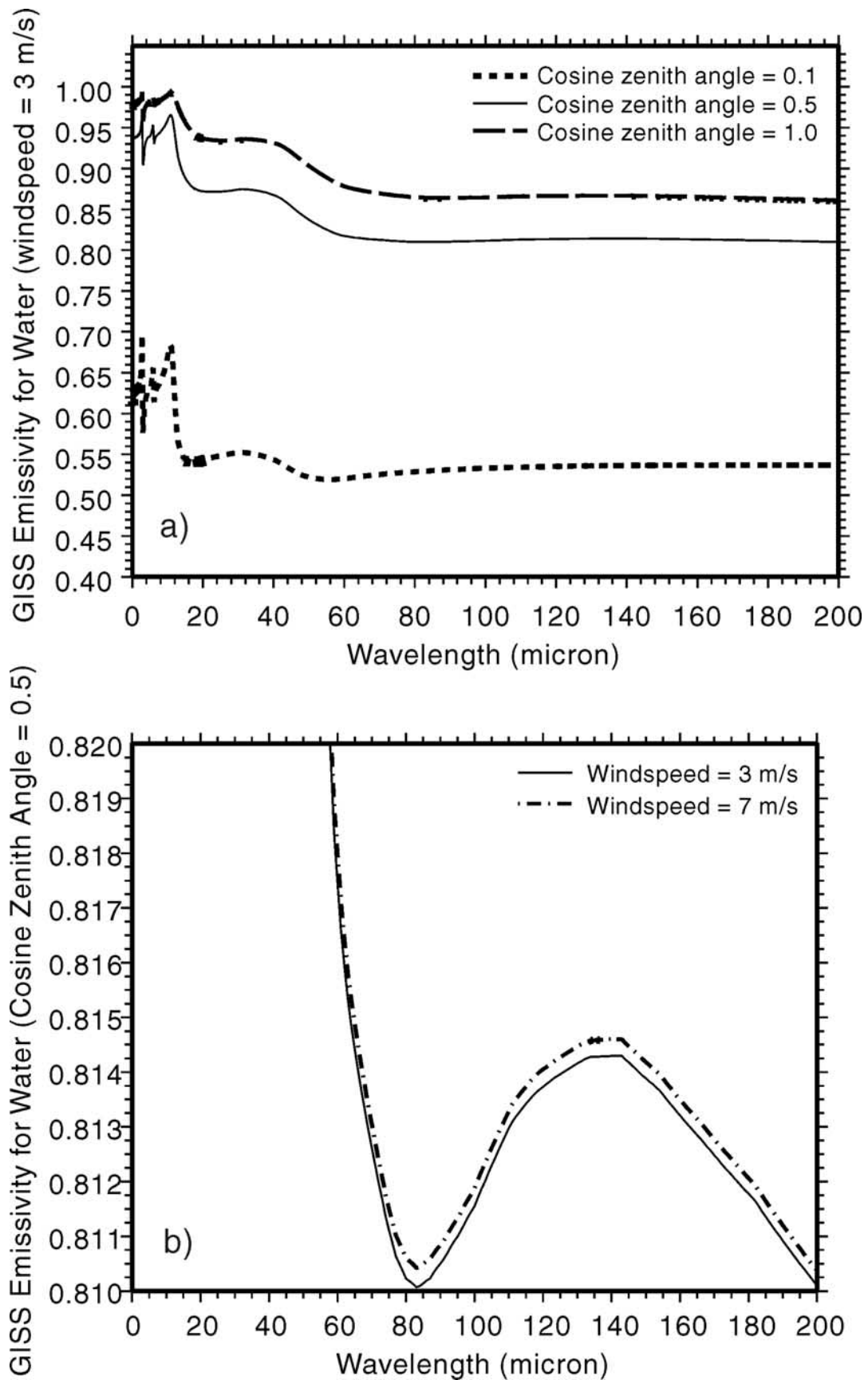
Figure 6. (a) Water emissivity from theoretical calculation using NASA GISS model (see text) at wind speed = 3 m/s for cosine zenith view angle = 0.1, 0.5, and 1.0. (b) Same as in Figure 6a but for a fixed cosine zenith view angle = 0.5 and for wind speed = 3 and 7 m/s.
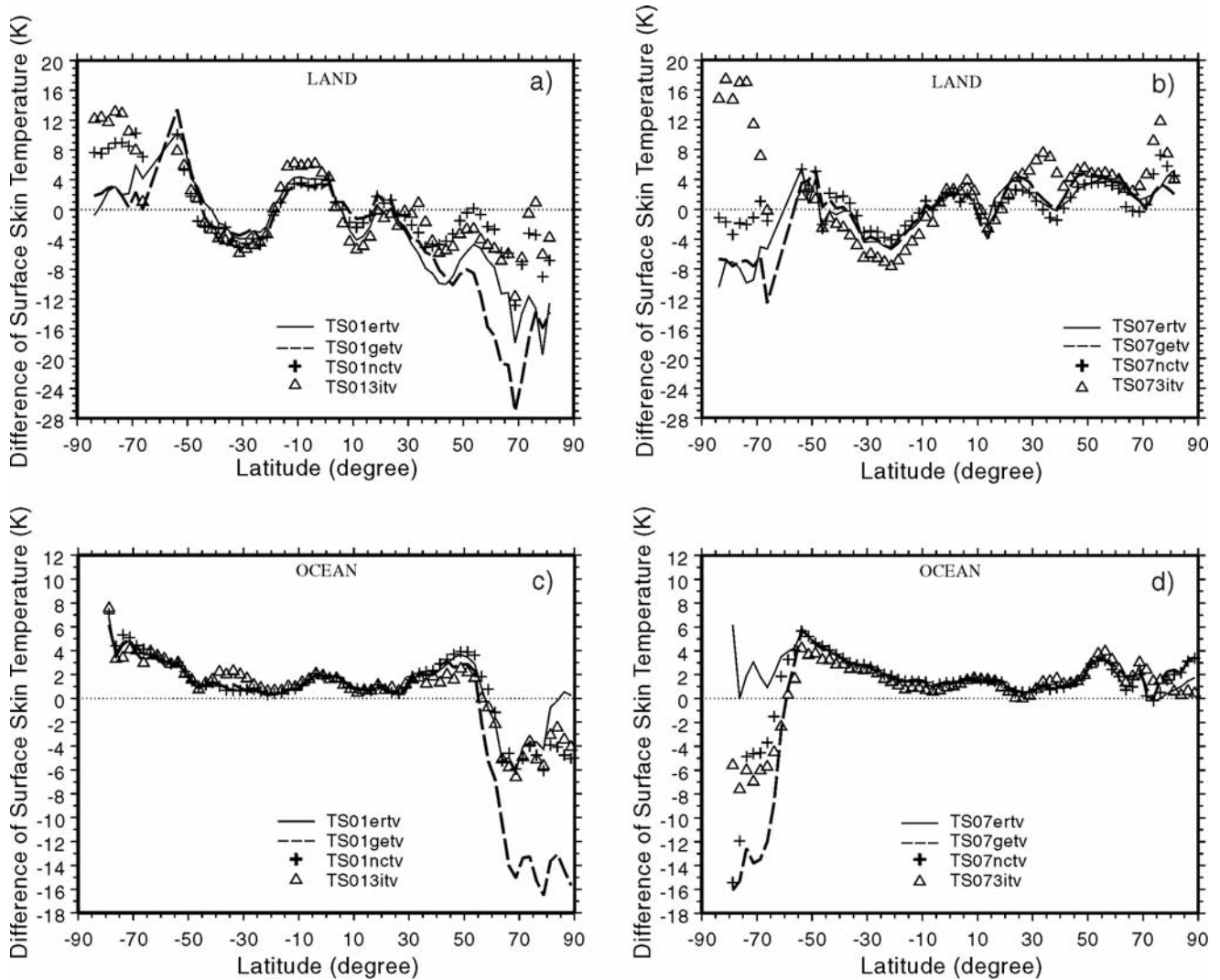
Figure 7. Global map of differences (ISCCP-FD minus SRB) of window region emissivities (in %) from ISCCP-FD 1992 annual mean and SRB climatology.

cancellation between land and ocean biases: If land and ocean are separated, the modulus mean (rms) difference of T_s is 1.57 (4.6) and 0.70 (2.4), respectively, compared with 0.73 (3.7) and 0.77 (1.9) for T_a. The land T_s modulus mean bias is twice that of T_a while the ocean values are comparable.

[33] Figure 8 illustrates the zonal monthly mean differences (all minus FDTV). The largest differences, up to 20 K, appear in the polar regions, where cloud contamination makes retrievals very difficult. In fact, wintertime polar regimes also exhibit larger clear-sky biases in T_s [cf. *Curry et al.*, 1996]. However, the reanalyses also exhibit the well-

Table 4. Comparison of Monthly Mean Surface Skin Temperature From ERA15, GEOS-1, NCEP, FDTV, and 3I for the Four Seasonal Months of 1992[a]

X/Y	Jan 1992		April 1992		July 1992		Oct 1992	
	Ocean	Land	Ocean	Land	Ocean	Land	Ocean	Land
ER/GE	0.57 (2.8)	1.21 (4.9)	0.33 (2.1)	−0.23 (3.8)	0.67 (3.4)	−0.27 (3.3)	0.70 (3.0)	0.94 (4.2)
ER/NC	−0.02 (0.9)	−2.72 (4.0)	0.12 (1.2)	−1.48 (4.0)	0.24 (1.7)	−0.27 (3.5)	0.33 (1.5)	−0.66 (3.6)
ER/TV	1.22 (2.7)	−3.52 (6.8)	1.68 (2.3)	−3.25 (5.3)	2.05 (2.1)	0.23 (5.4)	1.12 (2.7)	−2.89 (4.7)
ER/3I	−0.11 (1.8)	−1.46 (4.5)	0.27 (1.2)	−1.31 (4.8)	0.67 (2.2)	−0.79 (4.6)	0.37 (2.3)	−1.06 (4.0)
GE/NC	−0.60 (2.6)	−3.93 (5.9)	−0.21 (1.6)	−1.25 (2.8)	−0.43 (2.3)	0.00 (3.0)	−0.37 (2.1)	−1.61 (3.9)
GE/TV	0.64 (4.6)	−4.74 (8.6)	1.36 (3.1)	−3.02 (4.9)	1.38 (4.0)	0.50 (5.2)	0.43 (3.7)	−3.83 (5.0)
GE/3I	−0.68 (3.3)	−2.98 (6.4)	−0.06 (2.0)	−1.21 (4.8)	0.00 (2.3)	−0.84 (4.5)	−0.33 (2.7)	−2.33 (4.7)
NC/TV	1.24 (2.6)	−0.81 (5.4)	1.56 (2.4)	−1.77 (4.2)	1.81 (2.6)	0.49 (4.3)	0.80 (2.5)	−2.22 (4.6)
NC/3I	−0.08 (1.8)	0.85 (3.6)	0.15 (1.3)	−0.09 (3.9)	0.43 (1.6)	−0.95 (4.0)	0.04 (1.5)	−0.87 (3.3)
TV/3I	−1.32 (2.5)	1.95 (5.5)	−1.42 (2.2)	1.35 (4.8)	−1.38 (2.5)	−1.58 (5.8)	−0.75 (2.5)	1.48 (4.8)
Abs mean	0.65 (2.6)	2.42 (5.6)	0.72 (1.9)	1.50 (4.3)	0.91 (2.5)	0.59 (4.4)	0.52 (2.5)	1.79 (4.3)

[a]The numbers shown are global land/oceanic means and standard deviations of regional differences (X − Y) on a 280-km equal-area grid map in Kelvin. Ocean areas include coast cells (defined as area >33% of water; otherwise, land). "ER", "GE", "NC", "TV", and "3I" = are for ERA15, GEOS-1, NCEP, FDTV, and 3I, respectively. The ten X/Y pairs are all their possible combinations. The last row ("abs mean") is the modulus (i.e., absolute value) average of the mean differences (standard deviation) of the ten pairs, and it is not affected by the X/Y assignment. When averaging over all the four months of the last row, the pseudoannual/all-pair mean moduli (rms) differences = 0.70 (2.4) and 1.57(4.6) K for ocean and land, respectively. For the global (ocean and land) mean it becomes 0.52 (3.3) K.

Figure 8. (a) Difference of zonal monthly mean surface skin temperature (in K) for ERA15, GEOS-1, NCEP, and 3I minus FDTV (as TS01ertv for ER - TV, etc.) for land and January 1992. (b) Same as in Figure 8a but for July 1992. (c) Same as in Figure 8a but for ocean. (d) Same as in Figure 8b but for ocean.

known cold biases at these latitudes. For most lower and middle latitudes, the differences are generally ≲5 K and < 3 K for land and ocean, respectively. There is a systematic tendency for the reanalyses to be slightly colder in winter and warmer in summer over land relative to FDTV, despite the fact that the original ISCCP T_s retrievals have clear sky biases (too cold in winter, too warm in summer) [*Rossow and Garder*, 1993] that have been reduced in the FD analysis [*Zhang et al.*, 2004].

[34] We have collected three additional SST products: (1) NOAA/NASA Pathfinder Advanced Very High Resolution Radiometer (AVHRR) (descending and ascending) version 4.0 with 9 km/daily resolution and global coverage for 1981 to the current, produced by JPL/Caltech (estimated error is given as 0.5–0.7 K [*Vazquez et al.*, 1998]); (2) NOAA Optimum Interpolation Sea Surface Temperature Analysis version OI.V1 (1983–2000) and V2 (2000–2001) with 1°/weekly resolution and also global coverage [*Reynolds et al.*, 2002]; and (3) The Tropical Rainfall Measuring

Mission (TRMM) Microwave Image (TMI) version 3 with 25-km/weekly resolution and 40S–40N coverage for 1997 to 2004 [*Wentz and Meissner*, 2000] (also see comparisons given by *Chelton and Wentz* [2005]). The monthly mean time series for these data sets (simplified to "PF" for Pathfinder, "RS" for Reynolds, "WZ" for TMI, and "TV" for FDTV as before) are compared (after remapping them to the same 280-km equal-area map).

[35] Table 5 shows global averages of the statistical results from the SST time series comparison for all the individual 280-km cells for each of the six possible pairs of data. The correlation coefficients among the first three data sets (Pathfinder, Reynolds and TMI, value rows 1, 2 and 4) are all ≳0.96, despite very different space-time resolutions. The Pathfinder analysis procedure actually requires good agreement with the Reynolds data set. Their mean (rms) difference is ≲0.3 (0.3) K, reflecting the fact that all the three data sets are calibrated or regressed against the same in situ SST measurements, primarily buoys, to obtain "bulk"

Table 5. Global Mean Statistical Results From the SST Time Series Comparison for All the Individual 280-km Grid Cells for All the Possible Six Pairs From Four Data Sets[a]

X/Y	X	Y	M Diff	Standard Deviation	Correlation Coefficient	Slope	Intercept	Nm Dev
PF/RS	292.2 (1.7)	292.4 (1.6)	−0.28	0.32	0.958	0.913	25.54	0.22
PF/WZ	297.5 (1.6)	297.8 (1.6)	−0.28	0.29	0.973	0.992	2.79	0.20
PF/TV	292.2 (1.7)	291.3 (2.6)	0.82	1.60	0.712	1.168	−48.13	1.00
RS/WZ	297.7 (1.6)	297.8 (1.6)	−0.07	0.25	0.981	1.033	−9.93	0.16
RS/TV	292.2 (1.6)	291.1 (2.7)	1.11	1.70	0.689	1.217	−61.00	1.02
WZ/TV	297.8 (1.6)	296.0 (2.0)	1.72	1.06	0.786	1.047	−15.75	0.70

[a]As described in the text, the four data sets, Pathfinder, Reynolds, TMI, and FDTV, are denoted as PF, RS, WZ, and TV in the table. The statistical values are based on the coordinates of points in a scatterplot with Y values on the ordinate and X values on the abscissa. Regression statistics are from a linear least squares fit to the scatter of points. All values are in K, except the correlation coefficients and slopes, which are unitless. The first two value columns are mean (spatial standard deviation) for X and Y. "M Diff" ("stdv") is mean (rms) difference between X and Y, and "Nm Dev" is the rms distance of all the points from the regression line. The statistical results are from the compared time series for all the individual 280-km cells over the globe. All the data sets have a global coverage except WZ that only covers 40°S to 40°N ocean. The matched time periods vary from pair to pair with a maximum coverage from July 1983 to December 2003 (see text).

temperatures. The FDTV skin (not bulk) temperature values are less well correlated with these three data sets (correlations between 0.69 and 0.79 with larger mean (rms) differences, ranging from 0.82 (1.1) up to 1.7 (1.7)). The overall modulus mean (rms) difference is 0.71 (0.87), comparable to earlier comparisons in Table 4 (note that the reanalyses all use some version of the Reynolds SST). The high bias of the FDTV values (by about 1 K) may be accounted for, in part, by the difference between skin and bulk temperatures (the former is cooler on average by several tenths of degree at nighttime but can be significantly warmer during daytime), but as we show below it is more related to anomalies in the TOVS atmospheric temperatures used in the ISCCP retrieval. The larger variations of the FDTV values (standard deviation > 2 K compared with ≲1.6 K for the other three) is also associated in part with the larger variability (especially diurnal) of skin versus bulk temperatures.

[36] The zonal mean differences between these three SST data sets and FDTV for January and July 2000 (not shown) exhibit the same patterns as shown in Figure 8; that is, the biases between FDTV and the reanalyses (and 3I) are similar to those with the Reynolds SST, which is used in various ways as a standard for all the others. The larger polar differences are all associated with increasing sea ice fraction: The other SST products report water temperature, not the ice surface temperature as does FDTV. Excluding the polar regions, the difference between FDTV and the other data sets is generally ≲2 K. Figures 9a and 9b also show the differences in the SST anomaly time series (all minus FDTV) for global and tropical averages, respectively. Much of the large-amplitude variations of the other data sets relative to FDTV are induced in the ISCCP-retrieved T_s values by spurious temperature/humidity changes in the original TOVS as noted in the work of *Zhang et al.* [2006, section 2.1]).

[37] Because the difference of T_s and T_a controls the net LW at the surface, *Zhang et al.* [2006, section 2.9 and Figure 11] also compared the differences (T_s minus T_a) from FDTV with those from 3I and the three reanalyses but we do not repeat it here.

3. Summary and Discussion

[38] Estimating the surface radiation budget has long been pursued [*Simpson*, 1929] because, together with latent and sensible heat fluxes, it comprises one fundamental coupling of the atmosphere with the ocean and land surfaces. Direct estimates that resolve regional and weather-scale variability with reasonable accuracy have only become possible with the advent of complete global, mostly satellite, data sets within the past couple of decades. *Zhang et al.* [2004] now estimate that surface radiative fluxes can be determined to within about 10–15 W/m² (regional monthly mean flux values), improved by about 5 W/m² over *Rossow and Zhang* [1995]. The main limitation is still the accuracy of the input data sets. Sensitivity studies using ISCCP-based estimates ("realistically assumed") of the input uncertainties (based, in part, on the analysis presented here and in the work of *Zhang et al.* [1995, 2004, 2006]) show that the leading uncertainties in the surface fluxes are no longer predominantly induced by clouds but are now as much associated with uncertainties in the surface and near-surface atmospheric properties.

[39] This study presents a fuller, more quantitative evaluation of these uncertainties for the surface albedo and emissivity, and surface skin temperatures by comparing the main available global data sets that are treated as an ensemble of realizations of the actual climate such that their differences represent an estimate of the uncertainty in their values because we do not know the "truth". The results are globally representative and may be taken as a generalization of our previous ISCCP-based estimates from *Zhang et al.* [1995, 2004]. Generally speaking, the radiative flux uncertainties induced by the input uncertainties from *Zhang et al.* [2006] and this study are consistent with the flux uncertainty estimates by *Zhang et al.* [2004] based on all of our past and current sensitivity studies, and therefore in order to meet the accuracy requirements for climatological studies, say within 10 W/m², we still need substantial improvements of those input parameters that contribute major errors as summarized in the work of *Zhang et al.* [2006] and below.

[40] The main conclusions of this study, together with all the radiative flux sensitivity studies we have done previously, are as follows.

[41] 1. The uncertainty in global mean (rms) for regional differences for visible, NIR, and total SW black-sky albedo (land only) is 0.3% (7.5%), 16% (9%) and 7.6% (7%), respectively. Although land surface albedos in the NIR remain poorly constrained, they do not cause too much error in SW fluxes because the atmosphere absorbs much of the radiation in this wavelength range. Nevertheless, the subtle geographic and seasonal variations of surface
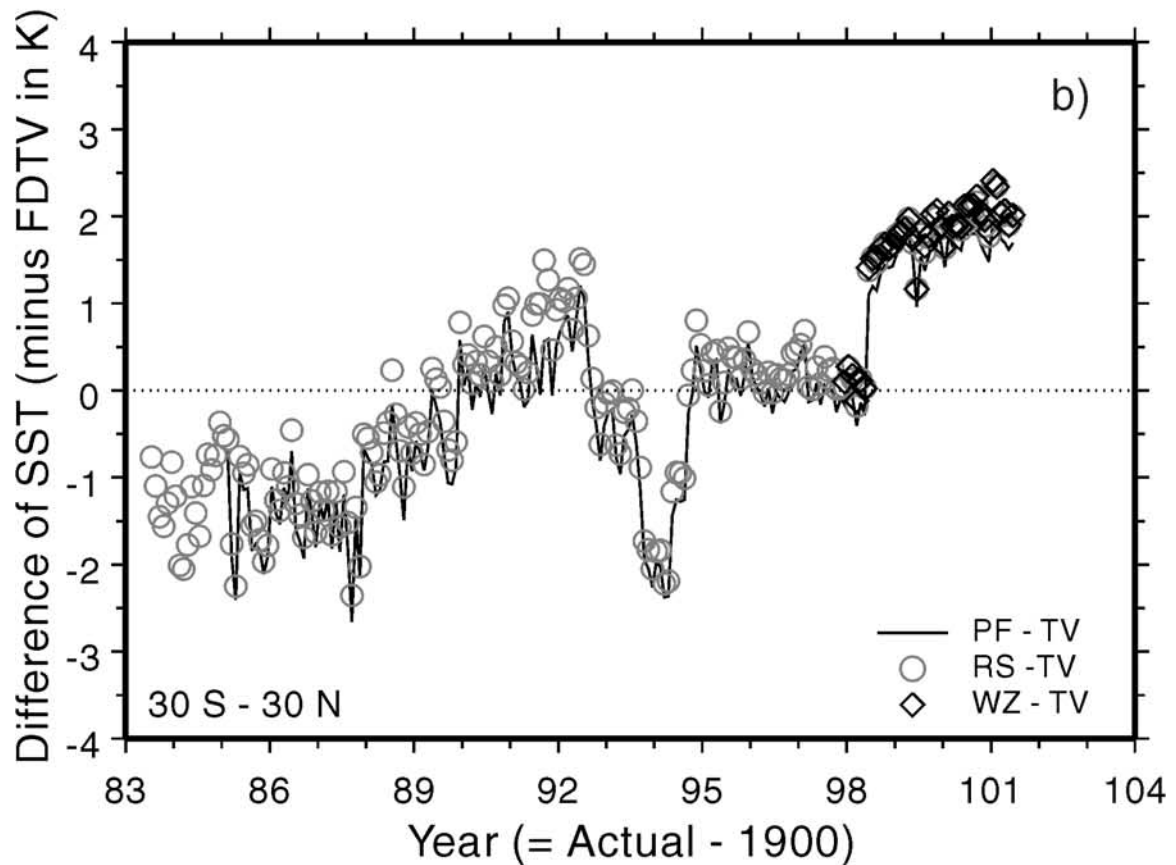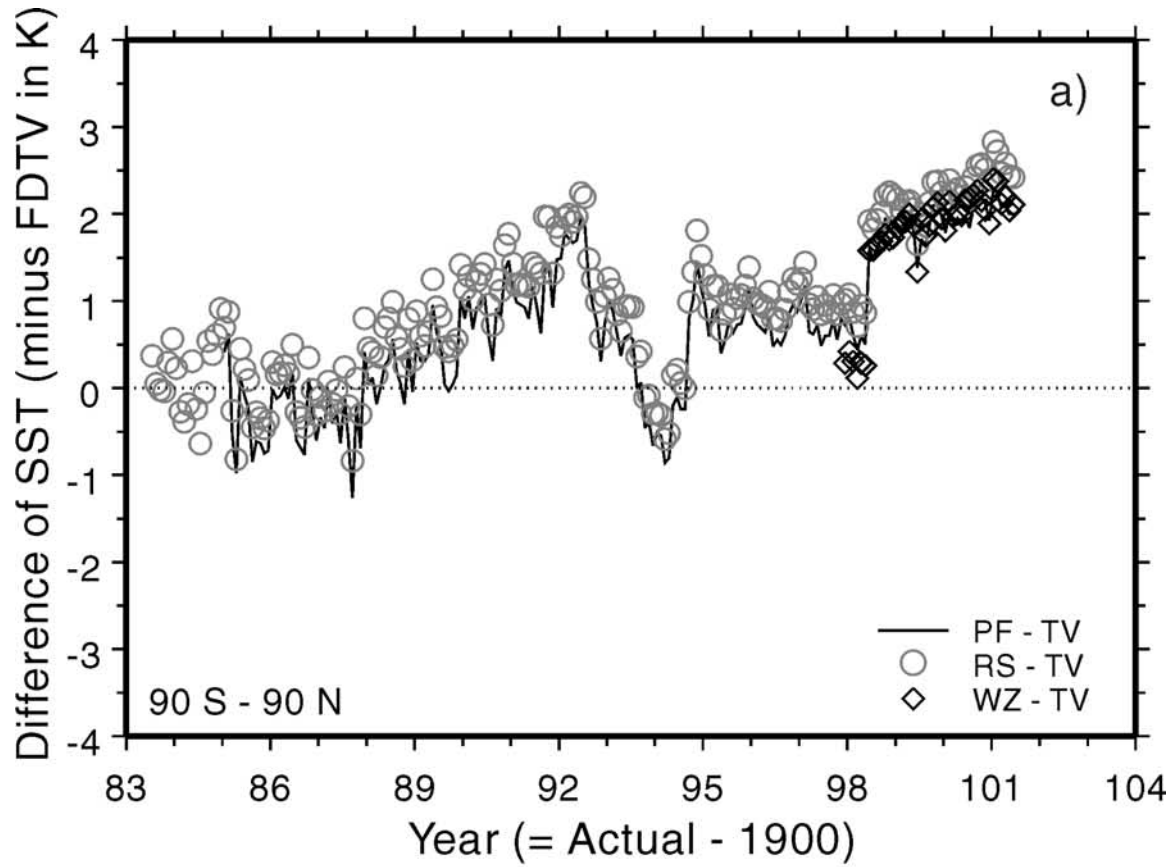
Figure 9. (a) Difference of the time series of global mean SST (in K) from Pathfinder (PF), Reynolds (RS), and TMI (WZ) minus FDTV (TV). (b) Same as in Figure 9a but for 30°S–30°N mean.

absorbed SW depend on variations of the NIR albedo influenced by the precise mixture of soil/rock, vegetation and snow and the seasonal variations of vegetation activity and snow. The mean (rms) difference of 7.6% (7%) in broadband black-sky SW albedo disagreement for land surface from this study leads to the uncertainty estimate of about 7%, which can easily induce $5-10$ W/m^2 uncertainty in (upwelling) surface SW flux estimates. However, the full potential of satellite sensors like MODIS or the Medium Resolution Imaging Spectrometer Instrument (MERIS) that sample (nearly) the complete solar wavelength range to produce definitive surface albedo maps with relatively high space-time resolution has not yet been achieved. The current 16-day period MODIS albedo, though having very high spatial resolution, is usually not globally complete. The current product is also produced with a 16-day time resolution. Most importantly, the current product corrects for atmospheric effects with a relatively crude climatology of atmospheric composition and aerosols: Neglecting the detailed space-time variations of water vapor, in particular, makes the uncertainties for the NIR albedo large. These limitations are not inherent; given the available data products specifying the ozone, water vapor and aerosol abundances as functions of location and time, a much more intensive analysis of the MODIS radiances is possible. However, to obtain the surface radiative fluxes over the whole time period of the ISCCP-FD product, the MODIS product must be used to ''calibrate'' the longer AVHRR record for surface albedo.

[42] 2. In the same way, the uncertainty for broadband and window emissivity may be taken as about $3-5\%$. Even though the disagreement between the two surface LW emissivity reconstructions appear to be relatively large, the fact that this disagreement is confined to wavelengths >20 μm means that it has little practical effect ($1-3$ W/m^2) on the surface upwelling LW fluxes because the atmosphere is nearly opaque at these wavelengths, so reflected downwelling radiation almost balances the reduction of upwelling radiation (this near balance is not true in the polar regions but there the fluxes are much smaller in magnitude).

[43] 3. The uncertainty in the skin temperatures is about 3 K. It is one of the two leading factors that cause problems with surface LW fluxes. Even though the disagreements among the various data sets are generally only $2-4$ K, this can easily cause $10-15$ W/m^2 uncertainty in surface (upwelling) LW calculation.

[44] The overall summary, based on both *Zhang et al.* [2006] and this work, is as follows. For surface LW fluxes, significant improvements could be obtained by improving the retrievals of (in order of decreasing importance): (1) surface skin temperature, (2) surface air and near-surface-layer temperature, (3) column precipitable water amount, and (4) broadband emissivity. As we have shown the retrieval of surface skin and air temperatures are linked because the relevant satellite measurements are sensitive to both so they should be retrieved together [cf. *Aires et al.*, 2002]. Moreover, the systematic differences between clear- and cloudy-sky skin temperatures require extension of the analysis of infrared measurements to include microwave measurements [cf. *Prigent et al.*, 2003]. Some improvement in surface emissivities over a limited wavelength range may come from a careful analysis of the new infrared spectrom-

eters, such as the Atmospheric Infrared Sounder (AIRS [see *Olsen*, 2005]). For surface SW fluxes, improvements could be obtained (excluding improved cloud treatment) by improving the retrievals of (1) aerosols (from our sensitivity studies but not discussed in this work) and (2) surface (black-sky) albedo, of which, NIR has larger uncertainty. Surface albedo and aerosols are also linked since satellite measurements at solar wavelengths are generally sensitive to both, especially over land, suggesting again, that the best results would be obtained by retrieving both together.

References

Aires, F., A. Chedin, N. A. Scott, and W. B. Rossow (2002), A regularized neural net approach for retrieval of atmospheric and surface temperatures with the IASI instrument, *J. Appl. Meteorol.*, *41*, 144–159.

Becker, F. (1987), The impact of spectral emissivity on the measurement of land surface temperature from a satellite, *Int. J. Remote Sens.*, *8*, 1509–1522.

Briegleb, B. P., P. Minnis, V. Ramanathan, and E. Harrison (1986), Comparison of regional clear-sky albedos inferred from satellite observations and model calculations, *J. Clim. Appl. Meteorol.*, *25*, 214–226.

Chelton, D. B., and F. J. Wentz (2005), Global microwave satellite observations of sea surface temperature for numerical weather prediction and climate research, *Bull. Am. Meteorol. Soc.*, *86*, 1097–1115.

Chen, C.-T., and E. Roeckner (1996), Validation of the Earth radiation budget as simulated by the Max Planck Institute for Meteorology general circulation model ECHAM4 using satellite observations of the Earth Radiation Budget Experiment, *J. Geophys. Res.*, *101*, 4269–4287.

Cox, C., and W. Munk (1956), Slopes of the sea surface deduced from photographs of the sun glitter, *Bull. Scripps Inst. Oceanogr.*, *6*, 401–488.

Csiszar, I., and G. Gutman (1999), Mapping global land surface albedo from NOAA AVHRR, *J. Geophys. Res.*, *104*, 6215–6228.

Curry, J. A., W. B. Rossow, D. Randall, and J. L. Schramm (1996), Overview of arctic cloud and radiation characteristics, *J. Clim.*, *9*, 1731–1760.

Darnell, W. L., W. F. Staylor, S. K. Gupta, N. A. Ritchey, and A. C. Wilber (1992), Seasonal variation of surface radiation budget derived from International Satellite Cloud Climatology Project C1 data, *J. Geophys. Res.*, *97*, 15,741–15,760.

Fu, Q., and K. N. Liou (1992), On the correlated k-distribution method for radiative transfer in nonhomogeneous atmosphere, *J. Atmos. Sci.*, *49*, 2139–2156.

Gibson, J. K.. P. Kållberg, S. Uppala, A. Hernandez, A. Nomura, and E. Serrano (1999), ERA-15 description, *ECMWF Re-analysis Proj. Rep. 1*, vers. 2, Eur. Cent. for Medium-Range Weather Forecasts, Bracknell, U. K.

Govaerts, Y. M., A. Lattanzio, B. Pinty, and J. Schmetz (2004), Consistent surface albedo retrieval from two adjacent geostationary satellites, *Geophys. Res. Lett.*, *31*, L15201, doi:10.1029/2004GL020418.

Gupta, S. K., D. P. Kratz, P. W. Stackhouse Jr., and A. C. Wilber (2001), The Langley parameterized shortwave algorithm (LPSA) for surface radiation budget studies, version 1.0, *Rep. NASA/TP-2001–211272*, 26 pp., NASA, Langley Research Center, Hampton, Va.

Hansen, J., G. Russell, D. Rind, P. Stone, A. Lacis, S. Lebedeff, R. Ruedy, and L. Travis (1983), Efficient three-dimensional global models for climate studies: Model I and II, *Mon. Weather Rev.*, *111*, 609–662.

Henderson-Sellers, A., and M. F. Wilson (1983), Surface albedo data for climate modeling, *Rev. Geophys.*, *21*, 1743–1778.

Jin, Y., C. B. Schaaf, F. Gao, X. Li, A. H. Strahler, W. Lucht, and S. Liang (2003a), Consistency of MODIS surface bidirectional reflectance distribution function and albedo retrievals: 1. Algorithm performance, *J. Geophys. Res.*, *108*(D5), 4158, doi:10.1029/2002JD002803.

Jin, Y., C. B. Schaaf, C. E. Woodcock, F. Gao, X. Li, A. H. Strahler, W. Lucht, and S. Liang (2003b), Consistency of MODIS surface bidirectional reflectance distribution function and albedo retrievals: 2. Validation, *J. Geophys. Res.*, *108*(D5), 4159, doi:10.1029/2002JD002804.

Kalnay, E., et al. (1996), The NCEP/NCAR 40-Year Reanalysis Project, *Bull. Am. Meteorol. Soc.*, 77, 437–471.

Kanamitsu, M. (1989), Description of the NMC global data assimilation and forecast system, *Weather Forecast.*, 4, 335–342.

Kistler, R., et al. (2001), The NCEP-NCAR 50 year reanalysis: Monthly means CD-ROM and documentation, *Bull. Am. Meteorol. Soc.*, 82(2), 247–267.

Lacis, A. A., and V. Oinas (1991), A description of the correlated k distribution method for modeling nongray gaseous absorption, thermal emission, and multiple scattering in vertically inhomogeneous atmospheres, *J. Geophys. Res.*, 96, 9027–9063.

Li, Z., and L. Garand (1994), Estimate of surface albedo from space: A parameterization for global application, *J. Geophys. Res.*, 99, 8335–8350.

Liang, S., A. H. Strahler, and C. W. Walthall (1999), Retrieval of land surface albedo from satellite observations: A simulation study, *J. Appl. Meteorol.*, 38, 712–725.

Liou, K. N. (2002), *An Introduction to Atmospheric Radiation*, 583 pp., Elsevier, New York.

Lucht, W., C. B. Schaaf, and A. H. Strahler (2000), An algorithm for the retrieval of albedo from space using semiempirical BRDF models, *IEEE Trans. Geosci. Remote Sens.*, 38, 977–998.

Matthews, E. (1982), Global vegetation and land use: New high-resolution data bases for climate studies, *J. Clim. Appl. Meteorol.*, 22, 474–487.

Matthews, E. (1985), Atlas of archived vegetation, land-use and seasonal albedo data sets, *NASA Tech. Memo., 86199*, 53 pp.

Matthews, E., and W. B. Rossow (1987), Regional and seasonal variations of surface reflectance at 0.6 μm, *J. Clim. Appl. Meteorol.*, 25, 170–202.

Olsen, E. T. (Ed.) (2005), AIRS/AMSU/HSB version 4.0 data release user guide, report, Jet Propul. Lab., Pasadena, Calif.

Peixoto, J. P., and A. H. Oort (1992), *Physics of Climate*, 520 pp., Am. Inst. of Phys., New York.

Pinker, R. T., and I. Laszlo (1992), Modeling surface solar irradiance for satellite applications on a global scale, *J. Appl. Meteorol.*, 31, 194–211.

Posey, J. W., and P. F. Clapp (1964), Global distribution of normal surface albedo, *Deofis. Int.*, 4, 33–48.

Prigent, C., W. B. Rossow, and E. Matthews (1997), Microwave land surface emissivities estimated from SSM/I observations, *J. Geophys. Res.*, 102, 21,867–21,890.

Prigent, C., J.-P. Wigneron, W. B. Rossow, and J. R. Pardo-Carrion (2000), Frequency and angular variations of land surface microwave emissivities: Can we estimate SSM/T and AMSU emissivities from SSM/I emissivities?, *IEEE Trans. Geosci. Remote Sens.*, 38, 2373–2386.

Prigent, C., F. Aires, and W. B. Rossow (2003), Land surface skin temperatures from a combined analysis of microwave and infrared satellite observations for an all-weather evaluation of the differences between air and skin temperatures, *J. Geophys. Res.*, 108(D10), 4310, doi:10.1029/2002JD002301.

Reynolds, R. W. (1988), A real-time global sea surface temperature analysis, *J. Clim.*, 1, 75–86.

Reynolds, R. W., N. A. Rayner, T. M. Smith, D. C. Stokes, and W. Wang (2002), An improved in situ and satellite SST analysis for climate, *J. Clim.*, 15, 1609–1625.

Rossow, W. B., and L. C. Garder (1993), Validation of ISCCP cloud detections, *J. Clim.*, 6, 2370–2393.

Rossow, W. B., and A. A. Lacis (1990), Global, seasonal cloud variations from satellite radiance measurements. part II: Cloud properties and radiative effects, *J. Clim.*, 3, 1204–1213.

Rossow, W. B., and R. A. Schiffer (1991), ISCCP cloud data products, *Bull. Am. Meteorol. Soc.*, 72, 1–20.

Rossow, W. B., and Y.-C. Zhang (1995), Calculation of surface and top-of-atmosphere radiative fluxes from physical quantities based on ISCCP data sets: 2. Validation and first results, *J. Geophys. Res.*, 100, 1167–1197.

Rossow, W. B., A. W. Walker, D. E. Beuschel, and M. D. Roiter (1996), International Satellite Cloud Climatology Project (ISCCP) documentation of new cloud data sets, *Rep. WMO/TD-737*, 115 pp., World Clim. Res. Prog., N. Y.

Salisbury, J. W., and D. M. D'Aria (1992), Emissivity of terrestrial materials in the 8–14 μm atmospheric window, *Remote Sens. Environ.*, 42, 83–106.

Schaaf, C. B., et al. (2002), First operational BRDF, albedo and nadir reflectance products from MODIS, *Remote Sens. Environ.*, 83, 135–148.

Scott, N. A., A. Chédin, R. Armante, J. Francis, C. Stubenrauch, J.-P. Chaboureau, F. Chevallier, C. Claud, and F. Cheruy (1999), Characteristics of the TOVS pathfinder Path-B data set, *Bull. Am. Meteorol. Soc.*, 80, 2679–2701.

Simpson, G. C. (1929), The distribution of terrestrial radiation, *Mem. R. Meteorol. Soc.*, 3, 53–78.

Stackhouse, P. W., S. K. Gupta, S. J. Cox, M. Chiacchio, and J. C. Mikovitz (1999), The WCRP/GEWEX Surface Radiation Budget Project release 2: First results at 1 degree resolution, paper presented at the 10th Conference on Atmospheric Radiation: A Symposium With Tributes to the Works of Verner E. Suomi, Am. Meteorol. Soc., Madison, Wis., 28 June–2 July.

Stackhouse, P. W., Jr., S. J. Cox, S. K. Gupta, M. Chiacchio, and J. C. Mikovitz (2001), The WCRP/GEWEX surface radiation budget project release 2: An assessment of surface fluxes at 1 degree resolution, in *IRS 2000: Current Problems in Atmospheric Radiation*, edited by W. L. Smith and Y. Timofeyev, pp. 485–488, A. Deepak, Hampton, Va.

Stackhouse, P. W., Jr., S. K. Gupta, S. J. Cox, J. C. Mikovitz, T. Zhang, and M. Chiacchio (2004), 12-year surface radiation budget data set, *GEWEX News*, 14(4), 10–12.

Staylor, W. F., and A. C. Wilber (1990), Global surface albedos estimated from ERBE data, paper presented at the 7th Conference on Atmospheric Radiation, Am. Meteorol. Soc., San Francisco, Calif.

Suttles, J. T., B. A. Wielicki, and S. Vemury (1992), Top of atmosphere radiative fluxes: Validation of ERBE scanner inversion algorithm using Nimbus 7 ERB data, *J. Appl. Meteorol.*, 31, 784–796.

Takacs, L. L., A. Molod, and T. Wang (1994), Documentation of the Goddard Earth Observing System (GEOS) general circulation model—Version 1, vol. 1, *NASA Tech. Memo., 104606*, 99 pp.

Vazquez, J., K. Perry, and K. Kilpatrick (1998), NOAA/NAA AVHRR oceans pathfinder sea surface temperature data set user's reference manual, *Publ. D-14070*, 67 pp., Jet Propul. Lab., Pasadena, Calif.

Wan, Z., Y. Zhang, Q. Zhang, and Z.-L. Li (2004), Quality assessment and validation of the MODIS global land surface temperature, *Int. J. Remote Sens.*, 25, 261–274.

Wentz, F. J., and T. Meissner (2000), AMSR ocean algorithm, *RSS Tech. Proposal 121599 A-1*, Goddard Space Flight Cent., Greenbelt, Md.

Whitlock, C. H., et al. (1995), First global WCRP shortwave surface radiation budget data set, *Bull. Am. Meteorol. Soc.*, 76, 905–922.

Wielicki, B. A., B. R. Barkstrom, E. F. Harrison, R. B. Lee, G. L. Smith, and J. E. Cooper (1996), Clouds and the Earth's Radiant Energy System (CERES): An Earth observing system experiment, *Bull. Am. Meteorol. Soc.*, 77, 853–868.

Wilber, A. C., D. P. Kratz, and S. K. Gupta (1999), Surface emissivity maps for use in satellite retrievals of longwave radiation, *NASA Tech. Memo., TP-1999-209362*, 30 pp.

Zhang, Y.-C., W. B. Rossow, and A. A. Lacis (1995), Calculation of surface and top-of-atmosphere radiative fluxes from physical quantities based on ISCCP data sets: 1. Method and sensitivity to input data uncertainties, *J. Geophys. Res.*, 100, 1149–1165.

Zhang, Y.-C., W. B. Rossow, A. A. Lacis, V. Oinas, and M. I. Mishchenko (2004), Calculation of radiative fluxes from the surface to top of atmosphere based on ISCCP and other global data sets: Refinements of the radiative transfer model and the input data, *J. Geophys. Res.*, 109, D19105, doi:10.1029/2003JD004457.

Zhang, Y.-C., W. B. Rossow, and P. W. Stackhouse Jr. (2006), Comparison of different global information sources used in surface radiative flux calculation: Radiative properties of the near-surface atmosphere, *J. Geophys. Res.*, 111, D13106, doi:10.1029/2005JD006873.

————————

W. B. Rossow, NASA Goddard Institute for Space Studies, 2880 Broadway, New York, NY 10025, USA.

P. W. Stackhouse Jr., NASA Langley Research Center, Hampton, VA 23681, USA.

Y. Zhang, APAM, NASA Goddard Institute for Space Studies, 2880 Broadway, New York, NY 10025, USA. (yzhang@giss.nasa.gov)